Ball bearing defect models: A study of simulated and experimental fault signatures

3 authors:

Chintamani Mishra
National Institute of Technology, Durgapur
11 PUBLICATIONS   244 CITATIONS

SEE PROFILE

Arun Kumar Samantaray
Indian Institute of Technology Kharagpur
215 PUBLICATIONS   3,257 CITATIONS

SEE PROFILE

Goutam Chakraborty
Indian Institute of Technology Kharagpur
70 PUBLICATIONS   916 CITATIONS

SEE PROFILE

Some of the authors of this publication are also working on these related projects:

Fault Diagnosis and Prognosis of Hybrid Dynamical Systems View project

Non-ideal drive systems View project

Ball bearing defect models: A study of simulated and experimental fault signatures

C. Mishra   A.K. Samantaray[1]   G. Chakraborty

Systems, Dynamics and Control Laboratory
Department of Mechanical Engineering, Indian Institute of Technology Kharagpur, 721302 Kharagpur, India

Abstract

Numerical model based virtual prototype of a system can serve as a tool to generate huge amount of data which replace the dependence on expensive and often difficult to conduct experiments. However, the model must be accurate enough to substitute the experiments. The abstraction level and details considered during model development depend on the purpose for which simulated data should be generated. This article concerns development of simulation models for deep groove ball bearings which are used in a variety of rotating machinery. The purpose of the model is to generate vibration signatures which usually contain features of bearing defects. Three different models with increasing level-of-complexity are considered: a bearing kinematics based planar motion block diagram model developed in MATLAB Simulink which does not explicitly consider cage and traction dynamics, a planar motion model with cage, traction and contact dynamics developed using multi-energy domain bond graph formalism in SYMBOLS software, and a detailed spatial multi-body dynamics model with complex contact and traction mechanics developed using ADAMS software. Experiments are conducted using Spectra Quest machine fault simulator with different prefabricated faulted bearings. The frequency domain characteristics of simulated and experimental vibration signals for different bearing faults are compared and conclusions are drawn regarding usefulness of the developed models.

Key words: Rolling element bearing; simulated vibration signature; fault diagnosis; bond graph; multi-body dynamics.

1. Introduction

Prompt detection of any incipient fault of in a critical component is important to avoid machine breakdown. Rolling element bearings are critical components in many rotating machineries. In these machines, vibration analysis is often used for condition monitoring of rolling element bearings. The bearing characteristics frequencies (BCFs) provide a theoretical estimation of frequency to be expected in the frequency spectra when there is any defect on parts of rolling element bearing. This assumes that an ideal impulse occurs when a rolling element strikes a fault-induced discontinuity on its rolling path. Depending upon the design parameters, many theoretical models of vibration generation mechanism are available. In the simplest form, kinematics based simplifications are employed to find the BCFs, which are functions of bearing geometric parameters, number of rolling

---

[1] Corresponding author: email: samantaray@mech.iitkgp.ernet.in, Tel: +91 3222 282998.

elements and frequencies of inner race and outer races. However, the vibration signal collected from the bearing system is contaminated by external noise, structural vibrations and external disturbances. The signal is therefore treated through many signal processing steps to remove noise and finally a diagnosis scheme (post processing step) is applied to characterise the frequency components in the vibration signal.

Often, the contact between rolling element and bearing races is discontinuous, and simple models based on continuous traction (no-slip) do not reproduce same qualitative vibration signal as that in a real industrial application. Likewise, models which do not explicitly model cage motion fail to replicate critical phenomena like bearing seizure. A model needs to be accurate enough to substitute experiments. The biggest advantage of having an accurate model is the ability to simulate various combinations of fault scenarios and generate corresponding responses, using which a knowledge-base can be generated to link various fault symptoms to their causes and finally, a root cause analysis system can be designed.

There is a lot of work reported on diagnosis of faults in rolling element bearings using vibration analysis [1, 2]. The vibration signatures used for analysis may be experimental or generated through simulation of appropriate models. Some important diagnosis schemes for diagnosis of rolling element bearings are high frequency resonance technique or envelope analysis [3, 4], time synchronous averaging [5], spectral kurtosis [6], higher order spectral technique [7], wavelet analysis [8, 9,10] and empirical mode decomposition [11].

The dynamics of rolling element bearing is affected by different operational and design parameters. However, it is almost impossible to replicate these parameters in an experimental study. So, a numerical model can be used to predict the behaviour of rolling element bearing under different parameters. The dynamic interaction of different parts, traction forces, slip and lubrication effects are generally considered while developing a mathematical model of a bearing. These models can be broadly divided into two types, i.e. quasi-static model and dynamic model [12]. In a quasi-static model, the force and moment equilibrium equations are considered whereas in a dynamic model, the differential equations of motion of each part of the rolling element bearing are considered. The dynamic model provides a time-domain transient simulation of the response of different parts of the bearing. Many works have been reported on the dynamic modelling of rolling element bearings [13]. Some important contributions in modelling of rolling element bearing dynamics pertain to formulations of differential equations of motion [14, 15], defect geometry modelling and evolution [16], and multi-body dynamics model [17,18].

There are many commercially available computer codes and multi-body dynamics simulation software which can be used to model rolling element bearings. Some difficult analyses like dynamic

analysis of cage behaviour in tapered roller bearing [19] and dynamic behaviour and resonance characteristics analysis [20] are reported using multi-body simulation (MBS) software ADAMS. Some of the commercial software dedicated towards dynamic analysis of rolling element bearings are BASDAP [14], SHABERTH [21], COBRA [22], DREB [23], ADORE [12], BEAST [16], CYBEAN [24] and CAGEDYN [25]. However, these specialized software are confined to only rolling element bearing analysis and cannot be coupled to models of machines or complex rotor systems as easily as can be done with MBS software. Rolling element bearing model, developed using multi-body system approach and vector bond graph form, where each rolling element, inner and outer races are modelled as six degrees of freedom system, is reported in [26]. The effects due to contact deflection forces, traction, gyroscopic and centrifugal forces, slip, contact separation, and localized fault were taken into consideration in that model whereas the effects due to cage dynamics was neglected. A model of rolling element bearing using planar multi-body dynamics formulation and bond graph approach is reported in [27], where the effects due to preload, unbalance, traction and cage dynamics are taken into consideration.

In this paper, three different models of ball bearing with increasing complexity and computational requirements are presented. The first is a 5-DOF model which is based on an earlier reported work in [28] and is implemented in MATLAB-Simulink environment. This model considers the effects due to preload and normal force due to ball race contact and neglects the effects due to traction forces. The second model is a more advance model based on an earlier reported work of these authors in [27] where multi-body dynamics approach is used to create a bond graph [29- 32] model of rolling element bearing. In addition to normal force and preload as in earlier model, the effects due to slip, cage dynamics and inertia of cage and ball are taken into consideration while developing the model. In those two works, the models of rolling element bearing are two-dimensional and only consider the dynamics of test bearing, whereas a rolling element bearing test rig consists of two or more bearings and a rotor shaft with few rotor disks. Thus, the third model of deep groove ball bearing with rotor shaft and disk is developed using 3-D multibody simulation (MBS) software ADAMS. These three models are used to extract the frequency domain features of a ball bearing in presence of different imperfections in its important parts. The ability of the developed models to reproduce similar frequency domain features under various bearing faults is evaluated by comparing the results with those obtained from experiments.

Before developing the models of deep groove ball bearing with various faults, the general layout of the experimental test rig is discussed in Section 2. Sections 3, 4 and 5, respectively, explain the 5-DOF Simulink model, bond graph model and ADAMS model of the system. Section 6 details the signal processing steps and the frequency domain fault diagnosis scheme used in this article. A comparative performance evaluation of the developed models under different fault scenarios is carried out in Section 7. Final conclusions and perspectives are drawn in Section 8.

2. Experimental setup

The machine fault simulator (MFS) developed by Spectra Quest, shown in Fig.1, is used to perform the experiments. It consists of an induction motor (Marathon, 3-phase, ½ HP), two aluminium pedestals, a loader, a coupling (Lovejoy), two ball bearings (1″ MB-ER-16K, Rexnord) and a variable frequency drive as its principal components.
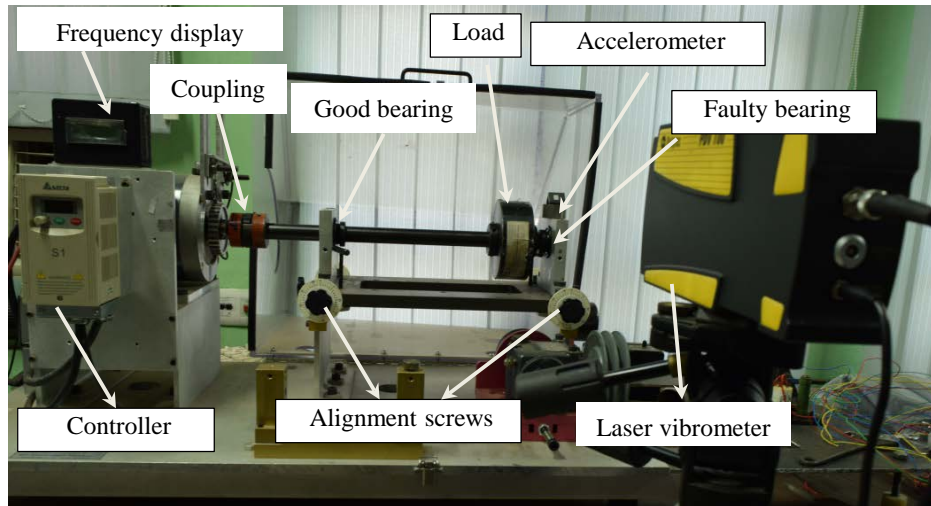

Fig.1. Machine fault simulator (MFS) system from Spectra Quest and its principal components.

An anti-vibration table is used to mount the MFS system. The output shaft of the motor is connected to driven rotor shaft by a flexible jaw coupling. The rotor shaft is supported by two deep groove ball bearings which are mounted on two aluminium pedestals. The first bearing is called load bearing and the second is called test bearing. The good bearing is installed at the near end whereas the test bearing/ faulty bearing is mounted at far end of the induction motor. Radial load is imparted to the test or outboard bearing by using a 5 kg rotor disc (called a loader) nearer to the test bearing. The speed of the driver shaft is regulated by variable frequency drive (VFD). For the present analysis, the control knob is manually adjusted to obtain a speed near 10 Hz. Different prefabricated faulted bearings such as with the fault in the outer race, inner race and ball are used as test bearings in the experiments.

Misalignment is one of the major defects in any rotating machine and it has its own vibration signature. A PRÜFTECHNIK make laser alignment system called OPTALIGN® smart RS5 is used here for precise alignment of the machine fault simulator. A Polytec make laser vibrometer is used to measure the velocity of pedestal that mounts the faulty bearing. A triangular log on the pedestal with a reflecting tape pasted on it is used as the test surface where the laser beam from the laser vibrometer is focused. This allows for measurement of a combined contribution of vertical and horizontal velocities of the test bearing pedestal. The inbuilt key-phasor of MFS system is used for measuring the averaged

shaft speed. An additional Brüel & Kjær (B&K) make accelerometer is used in the experiments. However, the velocities measured from the laser vibrometer are less noisy in comparison to the B&K accelerometer and are, thus, used in this study.

A data acquisition card (NI-USB-6211 A/D card with 16 channel 16 bit resolution) is used to acquire the pedestal vibration and the key-phasor pulse signals at a fixed sampling rate of 50000 Hz in a 10s time window. These data are then saved in the hard disc of a computer using LabVIEW interface. The schematic diagram of the measurement setup is shown in Fig. 2.
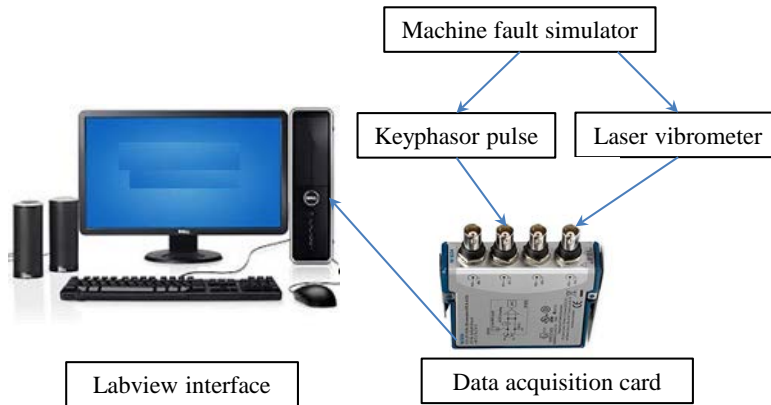
**Fig. 2.** Schematic diagram of data acquisition setup.

3. MATLAB-Simulink 5-DOF model of rolling element bearing

A simple MATLAB-Simulink model of bearing is developed here using the method proposed in [28]. The model considers the effects due to inertia of inner and outer races, contact force and localized fault. The inertia effects of cage and balls are neglected while developing the model. It is assumed in [28] and most other planar bearing models available in literature that the balls are somehow spaced at equal angular spacing and the balls and cage rotate at constant angular speeds. The outer race is connected to pedestal by a spring damper system representing structural parameters of the foundation, i.e., the bearing mounting. As in [28], an extra sprung mass system is included in the model to represent high frequency structural modes and it is used to simulate a typical high frequency resonant response of the bearing. Thus, the rolling element bearing system has five degrees of freedom with the inner and outer races having two degrees of freedom each and another degree of freedom is due to the sprung mass added to represent high frequency structural vibrations.

In this simplified bearing model (Fig. 3), the rotor is driven at constant velocity $\dot{\theta}_i = \omega_i$, the outer race is supported on a flexible support and the inner race is anchored to inertial frame through flexible supports (representing rotor shaft flexibility). In Fig. 3, M_P, K_P and R_P are support mass, stiffness and damping, respectively, M_S, K_S and R_S are equivalent rotor shaft mass, stiffness and damping,

respectively, K_R, R_R and m_R are stiffness, damping and mass of the sprung mass system, and K_b is the load-deflection factor of balls. The development of model is based on the following assumptions:

- The outer race does not rotate, the inner race rotates at constant speed,
- The contact between mating surfaces (ball and inner race, and ball and outer race) is considered as surface contact which follows Hertzian contact model,
- There is no slip between races and balls, and the balls always remain in contact with the races,
- There is constant angular separation between balls due to an ideal massless cage, and the balls are massless,
- All translational motions are in-plane ($x - y$ plane) and rotations are about z-axis.
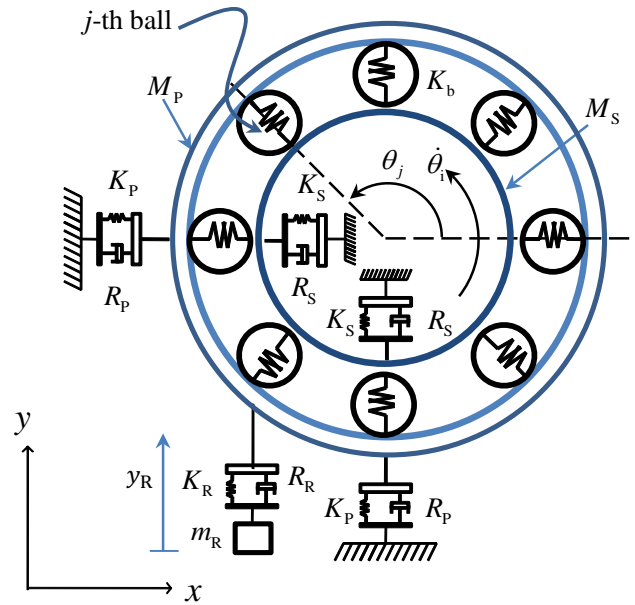
Fig. 3. 5-DOF model of bearing

The angular position of j-th ball, θ_j, as a function of cage angular speed ω_c ($f_c = \omega_c/2\pi$) is called fundamental train frequency or FTF), number of balls n_b, time elapsed t, and initial reference position θ_0 can be expressed as

$$\theta_j = \frac{2\pi(j-1)}{n_b} + \omega_c t + \theta_0. \tag{1}$$

From simple kinematic analysis of a deep groove ball bearing,

$$\omega_c = \frac{\omega_i}{2}\left(1 - \frac{d}{D}\right),$$

where D and d are, respectively, the pitch diameter of the bearing and the ball diameter. Note that ω_i and ω_c are expressed in rad/s in this article and the corresponding speeds in Hz are, respectively, given as f_s and f_c.

The bearing characteristic frequencies are defined in terms of geometric parameters of the bearing. For a deep groove ball bearing with zero contact/pressure angle and non-rotating outer race, they are given as follows:

$$\text{BPFI} = \frac{n_b f_s}{2}\left(1 + \frac{d}{D}\right),$$

$$\text{BPFO} = \frac{n_b f_s}{2}\left(1 - \frac{d}{D}\right),$$

$$\text{BSF} = \frac{f_s}{2}\left(\frac{D}{d}\right)\left(1 - \left(\frac{d}{D}\right)^2\right),$$

where BPFI, BPFO and BSF stand for ball pass frequency for inner race, ball pass frequency for outer race, and ball spin frequency and n_b, d and D are the number of balls, ball diameter and pitch diameter, respectively. The element defect frequency (EDF) is twice of BSF. These frequencies in Hz define the average value of how many times a specific fault would come in contact with any of the races in a unit time observation window.

3.1. Modelling contact

For contact deformation and angular position of j-th rolling element δ_j and θ_j, respectively, Hertzian contact force [33] in horizontal (F_x) and vertical (F_y) directions are written as

$$F_x = \sum_{j=1}^{N_b} K_b\, \delta_j^\gamma \cos\theta_j\,.\,h(-\delta_j), \tag{2}$$

$$F_y = \sum_{j=1}^{N_b} K_b\, \delta_j^\gamma \cos\theta_j\,.\,h(-\delta_j), \tag{3}$$

where, γ (3/2 for ball bearing and 10/9 for roller bearing) is the force exponent and the Heaviside function is given by

$$h(x) = \begin{cases} 1 & \text{for} \quad x \geq 0 \\ 0 & \text{for} \quad x < 0 \end{cases} \tag{4}$$

The contact deformation δ_j of j-th rolling element with clearance 'c' can be written as

$$\delta_j = x_d \cos\theta_j + y_d \sin\theta_j - c\,, \tag{5}$$

where, x_d and y_d are the relative displacement between inner race and ball for inner race fault and outer race and ball for outer race fault in x and y directions, respectively. For $\delta_j < 0$, the contact forces vanish. Note that traction or frictional forces are not modelled in the 5 DOF model.

3.2. Governing equations of motion

The pedestal (outer race) is modelled as a two degrees of freedom system that has translational motion in x and y directions. The equations of motion of the pedestal can be written as

$$M_P \ddot{x}_o = F_x - R_P \dot{x}_o - K_P x_o, \tag{6}$$

$$M_P \ddot{y}_o = F_y - M_P g - (R_P + R_R)\dot{y}_o - (K_P + K_R)y_o + K_R y_R + R_R \dot{y}_R, \tag{7}$$

where M_P is the pedestal mass, F_x and F_y are contact forces defined in Eqs. 2 and 3, x_o and y_o are x and y displacements of outer race center of mass (also geometric center), y_R is displacement of sprung mass, and g is acceleration due to gravity.

The inner race is fixed rigidly to the rotor shaft. It is two degrees of freedom system. It rotates with a constant angular speed. The equations of motion of the inner race can be written as

$$M_S \ddot{x}_i = -F_x + R_S \dot{x}_i + K_S x_i, \tag{8}$$

$$M_S \ddot{y}_i = -F_y - M_S g - R_S \dot{y}_i - K_S y_i, \tag{9}$$

where M_S is the mass of the rotor shaft with inner race, and x_i and y_i are x and y displacements of inner race center of mass.

The sprung mass is attached in y direction. Its equation of motion can be written as

$$M_R \ddot{y}_R = K_R(y_o - y_R) + R_R(\dot{y}_o - \dot{y}_R) - m_R g. \tag{10}$$

3.3. Modelling localised faults

Localised faults are modelled as proposed in [28]. Accordingly, constant angular width $(\Delta\phi_d)$ and depth (C_d) of the fault is assumed. Thus, the linear fault widths for inner, outer and ball fault are different. The fault models are the same for the 5-DOF simplified rolling element bearing model developed in this section and the bond graph model developed in the next section.

Outer race fault

A fault in the outer race is modelled as a small rectangular spall in the race (Fig. 4). When any ball approaches a specific angular position ϕ_d at which the balls' path encounters a spall on the outer race, there is a loss of contact and upon exiting this spall, the contact is established again. These sudden

contact losses and gains result in a large amount of periodic impulsive forces. The contact deformation in the case of outer fault can be calculated as

$$\delta_{\mathrm{o}} = \max(x_d \cos \theta_j + y_d \sin \theta_j - c - \delta_f, 0), \tag{11}$$

where $\delta_f = \begin{cases} C_d & \text{if} \quad \phi_d < \theta_j < \phi_d + \Delta\phi_d, \\ 0 & \text{otherwise.} \end{cases}$
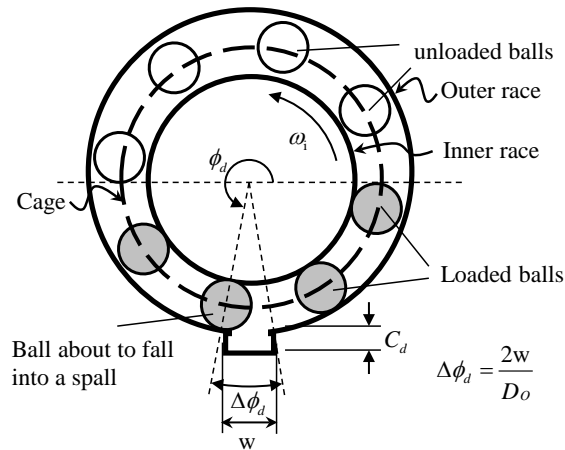
and $x_d = x_i - x_o, y_d = y_i - y_o.$

Fig. 4. Ball about to fall into a spall

Inner race fault

The inner race fault is modelled in similar way to that of in outer race. In case of inner race fault, the spall rotates with inner race and its position changes continually. Thus, ϕ_d value is dependent on the angle of shaft rotation which can be expressed as

$$\phi_d = \omega_{\mathrm{i}} t + \phi_0, \tag{12}$$

where ϕ_0 is the initial location of spall. For simulation, ϕ_d is modified by deducting full rotations out of it. The contact deformation is given as

$$\delta_{\mathrm{i}} = \max(x_d \cos \theta_j + y_d \sin \theta_j - c - \delta_f, 0), \tag{13}$$

where $\delta_f = \begin{cases} C_d & \text{if} \quad \phi_d < \theta_j < \phi_d + \Delta\phi_d, \\ 0 & \text{otherwise.} \end{cases}$

Ball fault

A spall in the ball rotates at the same speed as that of ball. At any instant, the angular position of the spall (See Fig. 5) can be expressed as

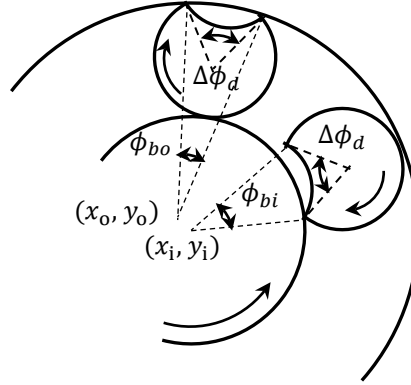$$\phi_s = \frac{\omega_i D}{2d}\left(1 - \left(\frac{d}{D}\cos\phi\right)^2\right)t + \phi_0 \tag{14}$$

where ϕ_0 is the initial position of spall. Note that the ball rotates in opposite direction to that of shaft rotation.

For ball fault, the angular width of ball fault in terms of inner and outer races (Fig. 5) can be expressed as

$$\phi_{bi} = \Delta\phi_d d/D_i, \tag{15}$$

$$\phi_{bo} = \Delta\phi_d d/D_o. \tag{16}$$

where D_i and D_o are the diameters of inner and outer races, respectively, and $D = (D_i + D_o)/2$.

Fig. 5. Fault angular width in terms of inner and outer races.

For each complete rotation of ball, loss of contact is detected twice, once contact with inner race is lost and once contact with outer race is lost. The inner race and the outer race have different curvatures and hence, the angular fault widths are different for the two contact losses. This difference in curvature also influences the depth of ball's entry into the spalls on the inner and outer races. The contact with the inner race is longer and deeper in comparison to that with the outer race.

When the rolling element (ball) is in contact with the inner race, the maximum depth to which the inner race enters the spall can be expressed as [28]

$$C_{di} = \frac{1}{2\left(D_i - \sqrt{D_i^2 - 4x^2}\right)}. \tag{17}$$

where x is the half spall width. When the spall is in contact with inner race, the inner race moves C_{di} downward while the rolling element moves upward by [28]

$$C_{dr} = \frac{1}{2(d - \sqrt{d^2 - 4x^2})}. \tag{18}$$

The net contact loss is then expressed as

$$C_d = C_{dr} + C_{di}. \tag{19}$$

Similarly, when the spall is in contact with outer race, the outer race will move towards its centre, i.e. inwards, whereas the rolling ball will move outwards. The net contact loss can be expressed as

$$C_d = C_{dr} - C_{do}, \tag{20}$$

where

$$C_{do} = \frac{1}{2\left(D_o - \sqrt{D_o{}^2 - 4x^2}\right)}. \tag{21}$$

This can be modelled by suitably changing the value of depth of the spall (C_d) for the faulty rolling element as

$$\delta_f = C_d = \begin{cases} C_{dr} - C_{do} & \text{if} & 0 < \phi_s < \phi_{bo}, \\ C_{dr} + C_{di} & \text{if} & \pi < \phi_s < \pi + \phi_{bi}, \\ 0 & & \text{otherwise.} \end{cases} \tag{22}$$

So, the overall contact deflection (contact deformation) in case of rolling element fault, where j-th rolling element is faulty can be expressed as

$$\delta_j = \max(x_d \cos \theta_j + y_d \sin \theta_j - c - \delta_f, 0), \tag{23}$$

3.4. Simulation setup

The equations of motion are solved in MATLAB-Simulink [34, 35] environment using ODE 45 solver with a relative tolerance of 1×10^{-4}. The parameters of 5-DOF model of bearing are given in Table 1. The parameters except the geometric parameters (geometric parameters of Rexnord MB-ER-16K 1″ deep groove ball bearing are used) of the model proposed in [28] are used in the simulation. The bearing characteristic frequencies (BCFs) using the geometric parameters of ball bearing are given in Table 2. The MATLAB-Simulink model of rolling element bearing is shown in Fig. 6. The forces on pedestal, rotor and sprung mass are shown in the left hand, right hand and bottom of the model. The mass of rotor, pedestal and sprung mass are denoted by ms, mp and mr, stiffness of rotor, shaft and sprung mass are denoted by ks, kp and kr and damping of rotor, pedestal and sprung mass are denoted by rs, rp and rr in the Simulink model.

Bearing Fault Simulation Model
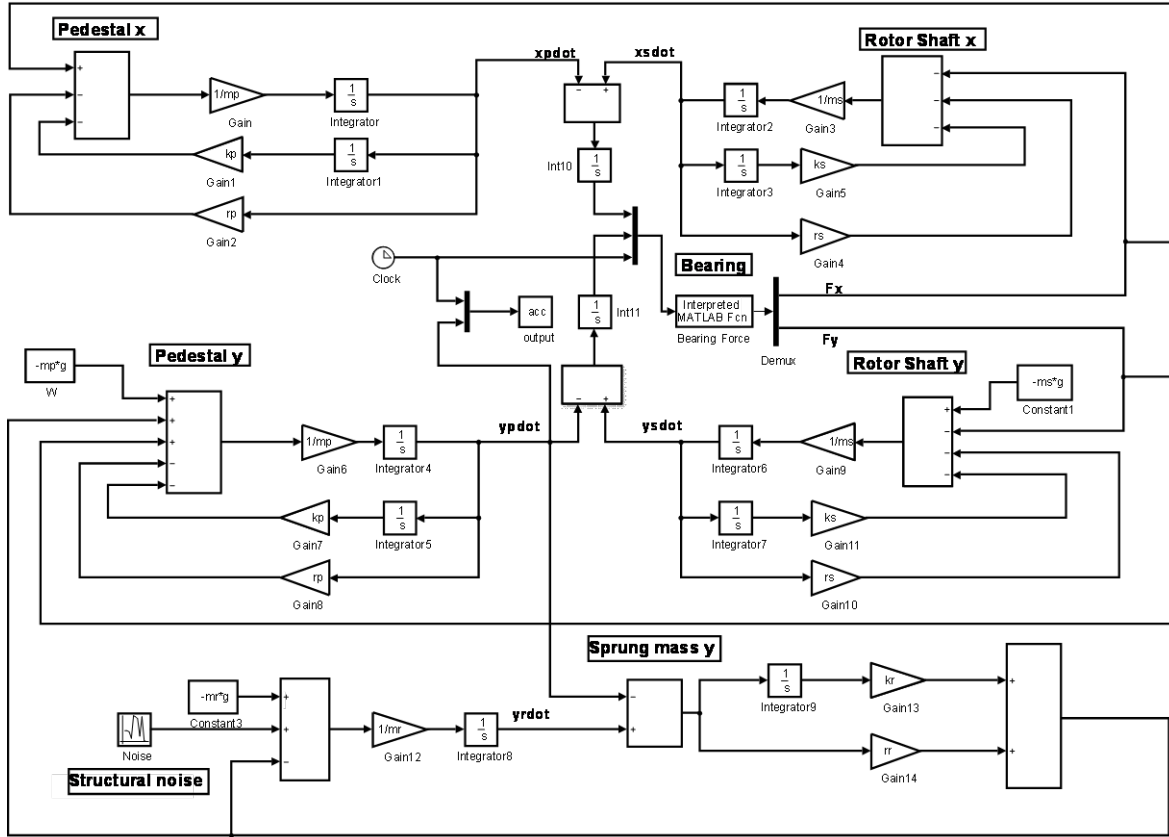
Fig. 6. MATLAB-Simulink model of rolling element bearing

A MATLAB function block is used to compute the contact forces F_x and F_y. The inputs to this block are the relative x and y displacements (x_d and y_d) and the simulation time. Fault conditions are included in the code of the MATLAB function. Additional noise source is included as an excitation on the sprung mass. The model output is the acceleration of the bearing pedestal (mount) in the vertical direction.

Table 1. Parameters of the rolling element bearing model

Parameters	Value
Stiffness of ball (K_b)	1.89×10^{10} N/m
Mass of pedestal (M_P)	12.638 kg
Stiffness of pedestal (K_P)	15.1×10^6 N/m
Damping of pedestal (R_P)	2210.7 Ns/m
Mass of shaft (M_S)	6.2638 kg
Stiffness of shaft (K_S)	7.42×10^7 N/m
Damping of shaft (R_S)	1376.8 Ns/m
Ball diameter (d)	7.94 mm
Pitch diameter (D)	39.32 mm
Fault depth (C_d)	1 mm
Fault width (w)	3 mm
Number of balls (n_b)	9

Table 2. Bearing characteristics frequencies of REXNORD MB-ER-16K deep groove ball bearing

Parameters	Value
Ball pass frequency of outer(BPFO)	$3.591\, f_S$
Ball pass frequency of inner(BPFI)	$5.408\, f_S$
Ball spin frequency(BSF)	$2.375 f_S$
Fundamental train frequency(FTF)	$0.399\, f_S$

4. Bond graph model of rotor bearing system

The second model in this article is a more advanced model developed using the bond graph [29-32] multi-body dynamics approach as proposed in [27] where in addition to localized faults, slip and traction forces at contact, motor torque, rolling element clearance and pre-compression, shaft unbalance and the cage dynamics are modelled. Note that the cage holds the rolling elements and maintains angular spacing between the rolling elements. Because this model includes cage dynamics, it can be used to study the cases involving loose rolling elements in the unloaded zone such as due to low preloading) and also to study bearing seizure due to say, heavy preloading or resistance to rolling element spin.

4.1. Model configuration

The rolling element bearing model considers inner race with rotor, bearing mount/ pedestal with the outer race, rolling elements (here, ball) and the cage as different bodies, which are rigid and move in a plane. The bearing mount and the rotor shaft are considered as flexible bodies [28]. The free body diagrams (FBDs) of the rigid body components in the model are given in Fig. 7. The torque applied to the motor shaft is represented by τ. The angular speed, stiffness and damping are represented by θ, K and R, respectively. The self-weight, reaction force and traction are, respectively, W, N and F. The subscripts used in Fig. 7, i, o, b, c, S, P, x and y represent the quantities for inner and outer races, ball, cage, rotor shaft, bearing pedestal, x direction and y direction, respectively. The ball contacts the inner and outer races within the grooves in a deep-groove ball bearing. The innermost portions of these grooves are shown by long dashes (hidden lines). The contact radii referred to in this article are the radii measured up to the groove's inner most points in the corresponding race.
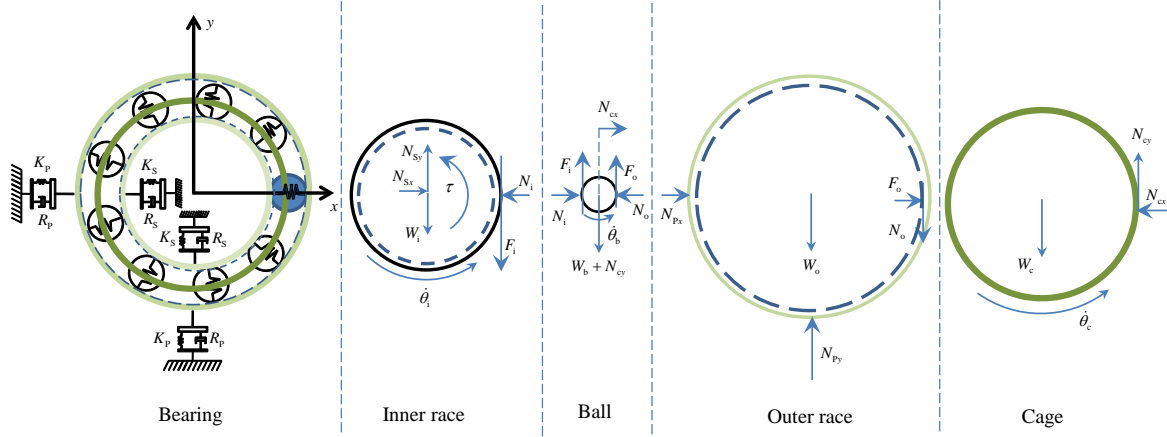
Fig. 7. FBDs of rigid body components of deep groove ball bearing in static equilibrium considering co-planar force system [26]. The contact and traction forces are shown with one representative ball. Under dynamic condition, the inertia forces will be also acting at the respective centres of mass.

The model considers planar motion for the inner and outer races, balls and the cage. The inner race, balls and the cage are allowed linear translation in x and y directions and rotation about z-axis (three degrees of freedom system). The other element, i.e., outer race permits translation in x and y directions with no rotation, hence has two-degrees-of-freedom.

The locations of instantaneous centers of cage, inner race, rolling elements and outer race are decided by dynamics of system. The model considers constrained motion of rolling element within the cage. Figure 7 shows the rolling element bearing as a spring-mass-damper system and free body diagram (FBD) of its different parts. The full model would include several rolling elements.

4.2. Contact and traction force modelling

The positions of all rigid bodies in the model are defined in the inertial reference frame ($x - y$ frame). The contact of a rolling element with the races, say that of j-th rolling element, is represented in Fig. 8. The positions of centre of inner race, outer race, and ball with respect to inertial frame are designated as $A(x_i, y_i)$, $B(x_o, y_o)$ and $C(x_b, y_b)$, respectively. It may be noted that the normal forces at the inner and outer race contact points are not collinear when points A and B are not coincident. The contact between inner race and j-th ball is at $P(x_P, y_P)$, and contact between outer race and ball is at $Q(x_q, y_q)$. The radius of inner race, outer race and ball are r_i, r_o and r_b, respectively, and the angular orientation of ball center with respect to inner and outer race centers are α and β, respectively.
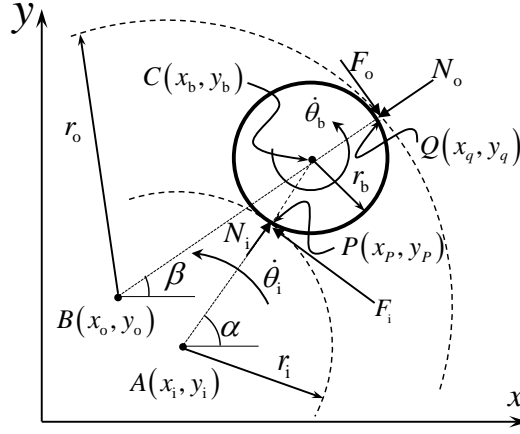
Fig. 8. The contact and traction forces at the interface between the ball and the races

The positions of the contact points P and Q, neglecting the small local deformations, can be written as

$$x_P = x_i + r_i \cos(\alpha), \ y_P = y_i + r_i \sin(\alpha), \tag{24}$$

$$x_Q = x_o + r_o \cos(\alpha), \ y_Q = y_o + r_o \sin(\alpha). \tag{25}$$

The velocity of point P on to the ball can be written as

$$\vec{V}_{Pb} = (\dot{x}_b \ \hat{\imath} + \dot{y}_b \ \hat{\jmath}) + \vec{\omega}_b \times \vec{r}_b. \tag{26}$$

where $\vec{r}_b$ is a position vector taken from ball center to the contact point and $\hat{\imath}$ and $\hat{\jmath}$ are the unit vectors in x and y directions, respectively. The same point's velocities on the inner race is given as

$$\vec{V}_{Pi} = (\dot{x}_i \ \hat{\imath} + \dot{y}_i \ \hat{\jmath}) + \vec{\omega}_i \times \vec{r}_i. \tag{27}$$

where $\vec{r}_i$ is a position vector taken from inner race center to the contact point and is counter-oriented to $\vec{r}_b$.

The frictional force between the ball and the inner race or outer race is due to slip, i.e., the tangential velocity difference. Under pure rolling, slip is zero and there is no traction force and no energy loss. It is assumed here that the bearing is lubricated and viscous friction dominates. If R_f is considered as the viscous resistance then the traction force on the ball at point P is given as

$$F_i = \left(R_f(\dot{x}_b - \dot{x}_i) \sin \alpha - R_f(\dot{y}_b - \dot{y}_i) \cos \alpha + R_f(\omega_b r_b + \omega_i r_i) \right) (-\sin \alpha \ \hat{\imath} + \cos \alpha \ \hat{\jmath}), \tag{28}$$

where $R_f = 0$ if $\delta \leq 0$ for the corresponding ball, and $\alpha = \tan^{-1}((y_b - y_i)/(x_b - x_i))$. For a perfect case of steady rolling of ball with no unbalance in the rotor shaft, $\omega_b r_b - \omega_i r_i = 0$. Thus, for small unbalance, simple kinematic analysis gives $\omega_b = (-r_i/r_b)\omega_i$ where the negative sign indicates that the rotation of the ball is in opposite direction to that of the rotor shaft, i.e., the inner race.

Generally, the bearing friction torque is due to tangential components of forces and it acts on the inner race. The frictional force arises out of deformation at contact, seal rubbing and lubrication. The lossescan be represented an effective resistance on the shaft rotation.

The normal force at the point of contact P is calculated assuming the surface contact between mating surfaces as

$$N = \begin{cases} K\delta^\gamma + R_b\dot{\delta} & \text{if } \delta > 0, \\ 0 & \text{otherwise,} \end{cases} \tag{29}$$

where N is the normal load, δ is the ball deformation and R_b is a small linear damping related to material/internal damping [28]. For inner race contact with the ball, $\delta = \sqrt{(x_b - x_i)^2 + (y_b - y_i)^2} - D/2$ where $D = D_i + d = 2(r_i + r_b)$ is the pitch circle diameter.

The normal and tangential forces at point Q can be represented likewise. The contact compression at the points of contact P and Q depend on the relative position of the ball with respect to the inner and outer race centres. These relative positions are influenced by inner and outer race motions and the cage rotation that governs the ball's angular position. The maximum deformation occurs in a ball when it is in the load zone (See Fig. 4).

4.3. Modelling localised fault

Commonly, rolling element bearing faults are caused by fatigue and fracture failures from wear and tear or due to incorrect operation such as large unbalance, shaft misalignment, etc. In most rolling element bearing fault models available in literature, raceway fault is modelled by a triangular or rectangular notch or a pit of regular shape in order to generate periodic/non-periodic impulses at constant/variable speed rotor operation [26, 27, 28 and 36]. The fault model for inner and outer race faults are discussed in Sec. 3.3 and the same is adopted here. Fault model proposed in [27], where the spall in the rolling element rotates with the rolling element is adopted for the rolling element fault.

Let, ϕ_s and ϕ_0 be the instantaneous and initial angular positions of the spall, respectively, where the angular position of the spall at any instant t is defined as

$$\phi_s = \int_0^t \dot{\theta}_b(\tau) d\tau + \phi_0 \tag{30}$$

Let, $\Delta\phi_d$ be the angular width of the spall subtended at the center of the rolling element. The positions of the starting and ending points (S$_1$ and S$_2$) of this spall (See Fig. 9) in the inertial reference frame are given by

$$\begin{aligned} x_{s1} &= x_b + r_b \cos\phi_s, & y_{s1} &= y_b + r_b \sin\phi_s \\ x_{s2} &= x_b + r_b \cos(\phi_s + \Delta\phi_d), & y_{s2} &= y_b + r_b \sin(\phi_s + \Delta\phi_d) \end{aligned} \tag{31}$$

Under dynamic loading conditions, the angular speeds of rotating parts (ball, cage and the inner race) are not constant due to the effects of slip and tangential and radial movement of raceways. Thus, the positions of points S_1 and S_2 are calculated by time integration of appropriate state variables [37]. Note that per one revolution of the faulty ball, there is once loss of contact with the outer race and once with the inner race.

The contact loss is found by the distance of points S_1 and S_2 to the centres of the inner and outer race and angle subtended by points S_1 and S_2 (See Fig. 9) at these race centres, i.e., (α_{s1} and α_{s2}) and (β_{s1} and β_{s2}). Due to difference in curvature, the duration of encounter with fault is different even for a constant rotor operating speed condition, i.e., $\alpha_{s2} - \alpha_{s1} \neq \beta_{s2} - \beta_{s1}$. Referring to Fig. 9, the ball spall is in contact with the outer race if $\beta_{s1} < \beta < \beta_{s2}$ or $\beta_{s2} < \beta < \beta_{s1}$ (a condition that accommodates forward and reverse rotations) and the points S_1 and S_2 are at a distance of more than the pitch circle radius from the outer race centre, i.e., the spall faces outwards. Likewise, the fault contact condition is defined for the inner race contact.

Due to difference in curvature of inner and outer races, they enter into the spall by different amounts. Here, C_{db} represents the average depth of entry into the spall. The fault modelling, as has been detailed in Sec. 3.3, is essentially representation of appearance and disappearance of intermittent clearance between the races and the faulty rolling element under the conditions mentioned above.

(a) (b)
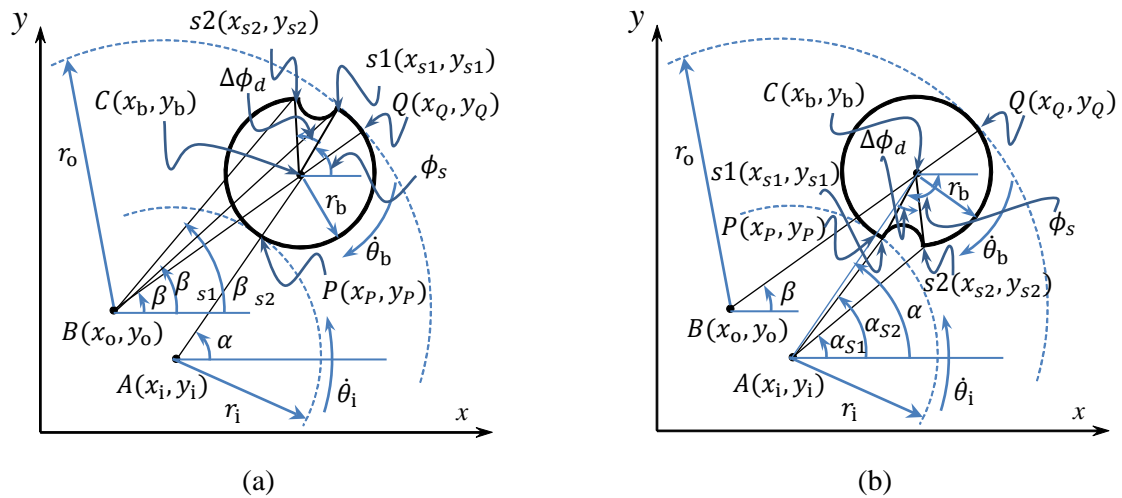
Fig. 9. Schema of a spall on the faulty ball. The races are in contact with fault when point P or Q lie within the spall, i.e., $\beta_{s1} < \beta < \beta_{s2}$ or $\beta_{s2} < \beta < \beta_{s1}$ for spall facing outer race and $\alpha_{s1} < \alpha < \alpha_{s2}$ or $\alpha_{s2} < \alpha < \alpha_{s1}$ for spall facing inner race [26].

4.4. Multi-body Dynamics Model Using Bond Graph

The model is developed here in a modular manner using the method proposed in [27], where bearing's two races, cage and all balls are modelled as separate sub-models.

Inner race sub-model

As in [28], it is assumed that the inner race is fixed to the ground (See Fig. 10 (a)) through a pair of spring-dampers in orthogonal directions, which represent the rotor shaft stiffness and damping. A torque or constant angular velocity source may be applied on the rotor shaft.

The center of mass is assumed to be at a small distance of e (eccentricity) from the shaft geometric axis, i.e. the spin axis. The instantaneous angular position of the mass center is θ_i and shaft angular speed is $\dot{\theta}_i = \omega$. In the inertial reference frame, the mass center (x_m, y_m) position is given by (refer to Fig. 10 (a))

$$x_m = x_i + e\cos\theta_i \quad \text{and} \quad y_m = y_i + e\sin\theta_i \tag{32}$$

where (x_i, y_i) is the position of the centre of the inner race. Thus, the velocity of the mass center is

$$\dot{x}_m = \dot{x}_i - e\dot{\theta}_i\sin\theta_i \quad \text{and} \quad \dot{y}_m = \dot{y}_i + e\dot{\theta}_i\cos\theta_i \tag{33}$$

Since the bond graph model will be developed in the inertial reference frame, it is not required to perform acceleration analysis. Note that the centrifugal forces and the additional polar moment of inertia (me^2) are automatically taken care of when the kinematics in Eq. (33) is represented in the bond graph model.

(a)   (b)
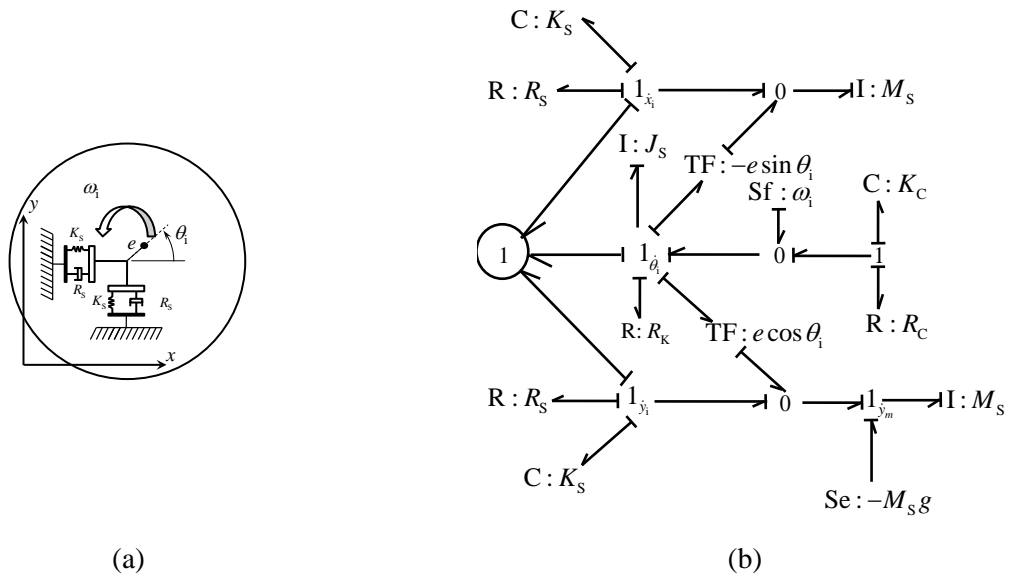
Fig. 10. (a) Representation of inner race of the bearing which combines the equivalent mass of the rotor disk and the stiffness and damping of the rotor shaft, and (b) bond graph sub-model of the inner race.

The inner race sub-model is shown in Fig. 10 (b) where the rotary inertia is modeled by $I : J_S$ and the spin resistance is modeled by $R : R_K$. The torsional stiffness and damping of the coupling between the motor and the rotor shaft are modeled by C: K_C and R: R_C, respectively. The equivalent mass of

the rotor disk, shaft and the race are modeled by $I:M_S$ in x and y directions, and the synchronous whirl bending stiffness and damping of the rotor shaft which are referred to the bearing end are represented with $C:K_S$ and $R:R_S$, respectively. The self-weight $Se:-M_S g$ is modeled at $1_{\dot{y}_m}$ junction. Two Tf elements and 0 junctions are used to model the kinematics in Eq. (33). The motor speed is model by $Sf:\omega_i$ where it is assumed that the motor gives a controlled speed. If the motor is assumed to provide a torque then $Sf:\omega_i$ and coupling model are replaced by an effort source (Se). This sub-model has a multi-bond interface port numbered as 1 (shown within a circle) to connect it with several rolling element sub-models.

Outer race sub-model

The outer race (See Fig. 11 (a)) is assumed to have no rotation. It is mounted on the bearing pedestal which has some structural stiffness and damping. Its sub-model is similar to that of the inner race and can be obtained from the later removing $1_{\dot{\theta}_i}$ junction of Fig. 10(b) and all connected parts (eccentricity model, and drive and coupling) and labeling the remaining junctions appropriately, to obtain the sub-model shown in Fig. 11(b).

In Fig. 11 (b), the equivalent mass, mounting structural stiffness and damping, and the self-weight are represented with $I:M_p$, $C:K_p$, $R:R_p$ and $Se:-M_p g$, respectively. For vibration analysis and bearing condition monitoring, the acceleration or velocity of the pedestal in the vertical direction is measured. Thus, an effort detector De (analogous to accelerometer when mass is constant) and a flow detector Df (analogous to velocity sensor) are implemented at appropriate locations in the model. A multi-bond interface port (port number 2) is used to connect this sub-model to the sub-models of rolling elements.

(a)   (b)
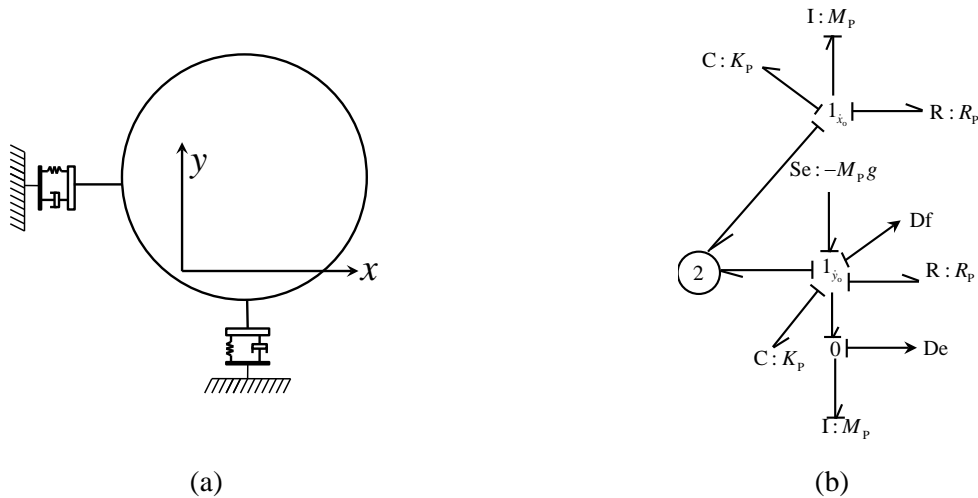
**Fig. 11.** (a) Representation of pedestal with outer race and (b) the bond graph sub-model of outer race.

Cage sub-model

The cage is modeled here as a 3 DOF rigid body whose primary purpose is to maintain a fixed angular spacing between the balls (Fig. 12 (a)). The actual cage has a space within which the balls are held. Here, we simplify that geometry and assume that the ball is attached to the cage through a revolute joint so that it can freely rotate about the axis of the pin-joint, i.e., an axis parallel to *z*-axis. This assumption holds because in a deep groove ball bearing, balls normally do not rotate about other axes. It is also assumed that a contact stiffness and damping exists to restrain relative translational between the ball and the cage. The clearance (like backlash) between the ball and the cage can be modeled by properly modifying the contact stiffness and damping element's constitutive relations.

In bond graph sub-model of the cage is given in Fig. 12 (b), where $I:J_c$, $I:M_c$ and $Se:-M_c g$, respectively represent the polar moment of inertia, mass and weight of the cage. For the *i*-th ball, the components of the velocity at the pin between the cage and the ball are

$$\dot{x}_{ji} = \dot{x}_c - r_c \dot{\theta}_c \sin\left(\theta_c + \frac{2\pi i}{n_b}\right) \quad \text{and} \quad \dot{y}_{ji} = \dot{y}_c + r_c \dot{\theta}_c \cos\left(\theta_c + \frac{2\pi i}{n_b}\right) \tag{34}$$

where $i = 0\dots(n_b - 1)$ is an enumeration of the balls with n_b being the number of balls, r_c is the pitch circle or mean radius, θ_c is the cage rotation angle, (x_c, y_c) defines the cage center position and (x_{ji}, y_{ji}) is the *i*-th ball center (i.e., pin or revolute joint) position on the cage.
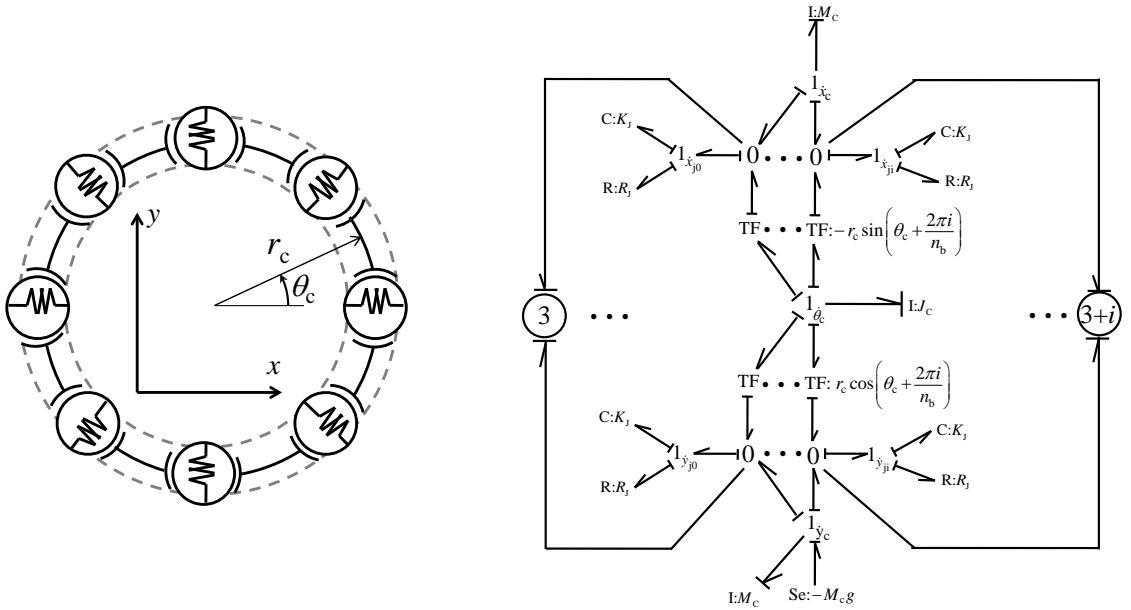

Fig. 12. (a) Schema of cage with rolling elements and (b) bond graph sub-model of cage.

The pin joint constrains the motion between the cage and the rolling element. In Fig. 12 (b), this constraint is modeled by flexible contact or pin flexibility through $C : K_j$ and $R : R_j$ elements and the kinematic relation given in Eq. (34) is represented through two TF elements and other junction structures. The cage sub-model is interfaced to n_b number of sub-models for rolling elements through n_b number of multi-ports numbered 3 to $3 + (n_b - 1)$.

Rolling element/Ball sub-model

The bond graph sub-model of rolling element (here, ball) is shown in Fig. 13. It has two non-linear contact springs ($C : K_b$), two linear contact dampers ($R : R_b$) and two dampers ($R : R_f$) for friction/traction force modeling. The sub-models of inner and outer races (See Figs. 10 and 11) are connected to rolling element sub model by interface ports 1 and 2, respectively. The interface port $3 + i$ $(i = 0 \ldots (n_b - 1))$, connects the i-th rolling element/ball to the cage sub-model. The other variables are self-weight, rotary inertia and linear inertia, which are modelled by elements $Se : -M_b g$, $I : J_b$ and $I : M_b$, respectively. The non-linear contact force and traction forces including contact and traction loss are modeled according to Eqs. (28) and (29) as formulated in Section 4.2. Note that the traction force is responsible for spin of balls as well as rotation of the cage.
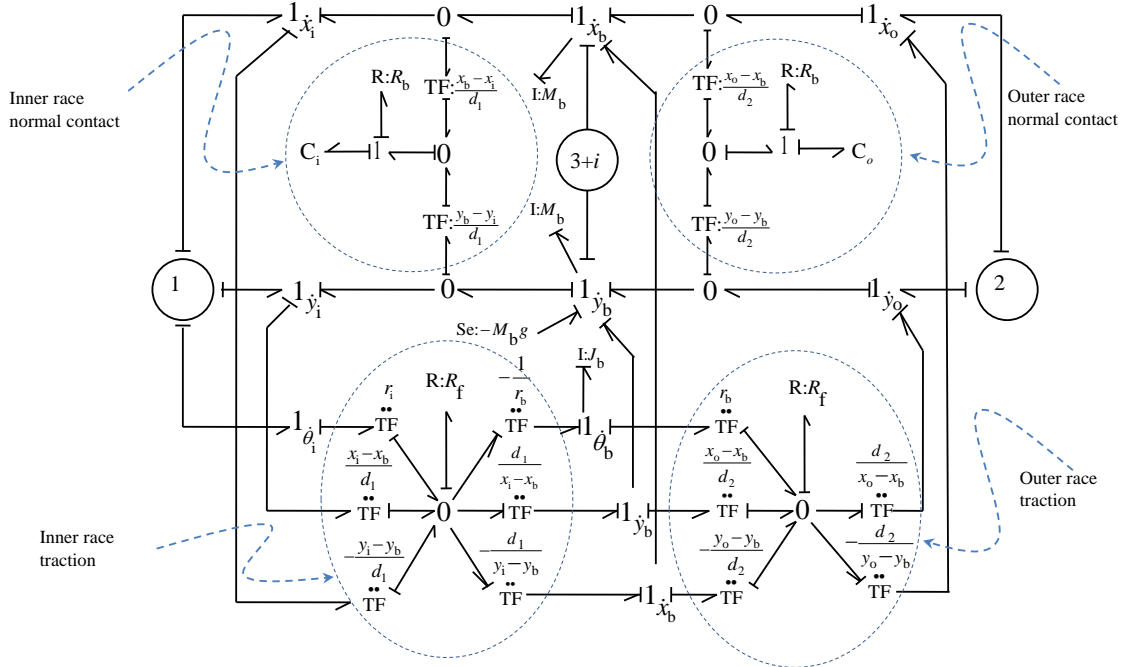
Fig. 13. The bond graph sub-model of a ball.

The instantaneous distance between the ball and inner race centers is $d_1 = \sqrt{(x_i - x_b)^2 + (y_i - y_b)^2}$ i.e.

$$d_1^2 = \left(x_i - x_b \right)^2 + \left(y_i - y_b \right)^2 \tag{35}$$

Taking time derivatives of both sides,

$$2d_1\dot{d}_1 = 2\left(x_i - x_b \right)\left(\dot{x}_i - \dot{x}_b \right) + 2\left(y_i - y_b \right)\left(\dot{y}_i - \dot{y}_b \right)$$

or

$$\dot{d}_1 = \frac{\left(x_i - x_b \right)}{d_1}\left(\dot{x}_i - \dot{x}_b \right) + \frac{\left(y_i - y_b \right)}{d_1}\left(\dot{y}_i - \dot{y}_b \right) = \left(\dot{x}_i - \dot{x}_b \right)\cos\alpha + \left(\dot{y}_i - \dot{y}_b \right)\sin\alpha. \tag{36}$$

The above kinematic equation is represented in the ball sub-model using two transformers whose moduli are the two direction cosines. Here, time integration of $\dot{d}_1$ with appropriate initial condition gives the ball compression and the contact forces are calculated using Hertzian contact formulation (See Eq. (29)). Likewise, the instantaneous distance between the ball and outer race centers is denoted by $d_2 = \sqrt{\left(x_o - x_b \right)^2 + \left(y_o - y_b \right)^2}$ and the corresponding kinematic relations are modeled using two more transformers. The transformer moduli are $\cos\alpha = \left(x_i - x_b \right)/d_1$, $\sin\alpha = \left(y_i - y_b \right)/d_1$, $\cos\beta = \left(x_o - x_b \right)/d_2$, and $\sin\beta = \left(y_o - y_b \right)/d_2$, where the angles α and β are explained in Fig. 2. Note that the state variables (positions of two races and all ball centers) must be appropriately initialized taking into account the ball clearance/pre-compression, number of balls and their initial positions. Distanced d_1 and d_2 are also state variables which are associated with C_i and C_o elements of the sub-model, respectively.

The traction between the ball and inner race is governed by Eq. (28) which is modeled using six transformer elements and the resistance R: R_f. The traction between the ball and the outer race is modeled likewise.

Integrated model of rolling element bearing

Different sub models are connected through interface ports to obtain the complete bond graph model of the deep-groove ball bearing (Fig. 14). The measurement extracted from the model is the vertical velocity of the bearing mount, i.e., the outer race. Gaussian white noise is added to the measurement to contaminate the output signal and simulate a more practical measurement signal where the fault symptoms get fully or partially buried within the noise.

The bond graph sub-models are developed as capsules of SYMBOLS [38, 39] software. SYMBOLS software is a suite of applications that provide a set of tools for bond graph and block diagram model building in a graphical interface, numerical simulation, post processing in time and frequency domain, control theoretic analysis and fault diagnosis [40]. The bond graph sub-models are assembled to generate the global model. SYMBOLS software assigns causalities and then generates the state space equations which are integrated using Runge-Kutta-Fehlberg (RK4.5) method.
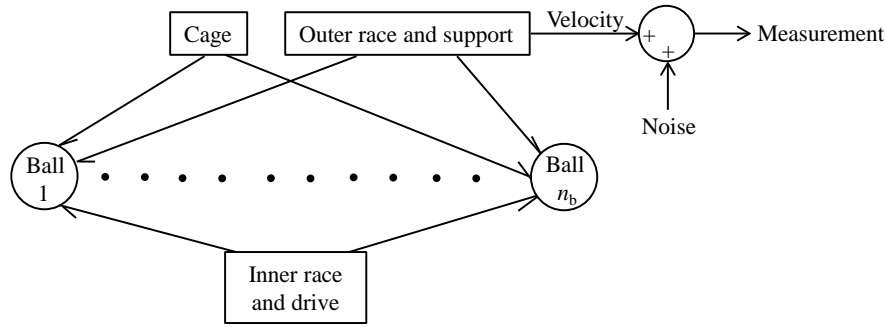
Fig. 14. The word bond graph model of deep groove ball bearing composed of basic sub-models.

4.5. Model data

The geometric parameter corresponding to (MB-ER-16K 1" bearing are used for model simulation. The self-weight of the rotor and rotor shaft is considered as the radial load. A small eccentricity of 100 μm is considered in the rotor disk. The additional parameter values in the model are listed in Table 3 where the mass parameters (mass and rotary inertia) are computed using solid models and material density. The values of stiffness parameters are selected in such a way that a frequency response (FRF) similar to that found from the experiments is obtained. Note that the structural resonance zone in FRF of simulated and real systems need to match approximately so that the same band-pass filter can be applied to both while performing envelope analysis for fault diagnosis. The damping values are optimized to speed-up the simulations and aid in convergence.

Table 3. Mass, stiffness and damping of ball, pedestal, cage with pin and shaft

Part	Mass (kg)	Stiffness/ Load deflection factor	Damping	Polar M.I.$(kg.m^2)$
Ball	0.002	9. 2×10^8 N/m$^{3/2}$	1000 Ns/m	1.26×10^{-8}
Pedestal and outer race	3	4×10^7 N/m	1000 Ns/m	—
Cage and pin	0.06	1×10^8 N/m	1 Ns/m	0.005
Rotor shaft and inner race	11.213	0 N/m	0 Ns/m	1
Flexible Coupling	—	1×10^4 Nm/rad	100 Nms/rad	0

5. Multibody CAD model of rolling element bearing using MBS software ADAMS

In the previous sections, different analytical models of rolling element bearings have been discussed. However, it becomes very difficult to model different types of imperfections such as ball over size, elliptical ball, elliptical cage, etc. using analytical models. Moreover, the profiles of faults assumed in 2-D models are uniform in shape. In 3-D simulation software, we can model different profiles of faults like those occurring in the real industrial scenario due to wear, indentation, smearing, surface

distress, corrosion, flaking, cracks etc. A comprehensive chart of different types of bearing faults and the reasons for the faults can be found in SKF bearing damage chart. To model such types of defects, a multi-body simulation commercial software Adams is used here, where we can introduce different types of damages in the elements of bearing in component CAD models. In model development, a complete model of the test-rig including the rolling element bearing (here, deep groove ball bearing), which is first of its kind, has been developed using MBS ADAMS (Fig. 15).
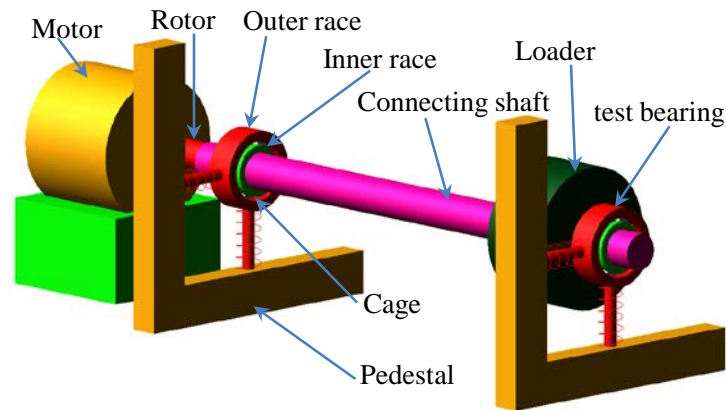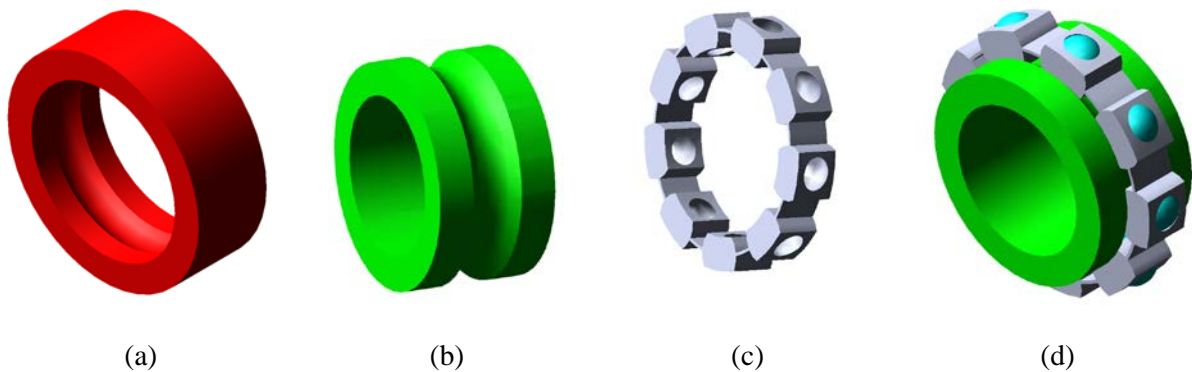

Fig. 15. ADAMS MBS model of deep groove ball element bearing test rig.

5.1. Modelling of important parts

The inner race, outer race, ball and cage of the model are considered as rigid bodies. The traction between elements, non-linear contact stiffness and damping, slip, imperfections due to manufacturing and faults are all included in the model.

| (a) | (b) | (c) | (d) |

**Fig. 16.** CAD model of (a) outer race, (b) inner race and (c) cage and (d) inner race with cage and balls

The model of the test rig consists of a rotor shaft connected to the motor through a flexible coupling, which offers significant torsional stiffness, but low bending stiffness in order to accommodate parallel and angular shaft misalignments. The rotor shaft is rigid both in torsion and bending. The flexible coupling is designed in the model by attaching a bushing between the rotor and

motor shafts. A small parallel misalignment of 1 mm is introduced in the model by shifting the axis of rotor and axis of connecting shaft of the motor. The rotor shaft is supported by two deep groove ball bearings which are mounted on two pedestals. Like the experimental setup, a good bearing is installed in the near end and the faulty/test bearing is mounted at the far end of the motor. The inner races of the bearings (Fig. 16 (b)) are constrained to move with the rotor shaft by attaching a fixed joint (ADAMS nomenclature for the constraint) between the rotor shaft and the inner race. A loader is attached near the test bearing to impart radial load. The motion of the loader is constrained by fixed connection/joint between the rotor shaft and loader.

The outer races (Fig. 16 (a)) are connected to spring damper systems in horizontal and vertical directions in order to model structural stiffness and damping of bearing mounts. To resist the axial forces and moments on the outer race, a bushing with high stiffness and damping in the three mutually perpendicular directions to both bearings is used between the outer races and the corresponding pedestals. These bushings are not shown in Fig. 16(a) to maintain clarity of the figure. The cage (Fig. 16 (c)) is modelled as a floating body which accommodates balls at constant angular spacing. The cage does not contact with the inner as well as outer races. The bearing model permits slip between the ball and races, and ball and cage. It is modelled by giving suitable parameters in definition of contact force between the connecting bodies. The calculations of contact and friction forces are given in the next section. The balls (Fig. 16 (d)) are modelled as rigid bodies which are held inside the cage. Contact constraints are defined between each ball and the cage which permits a small play (clearance) between each ball and the cage groove. Likewise, contact constraints are defined between each ball and both the inner and outer races.

5.2. Modelling of contact and frictional force

The contacts between the balls and races and ball and cage are considered to be of solid to solid type. The contact stiffness and damping are determined using Hertzian contact theory, in which the load deflection factor is dependent on the curvatures of the mating surfaces and the material parameters. The tangential forces are defined using Coulomb friction model. As per ADAMS implementation, three values of coefficients of friction at the contact point for slip velocity, less than the static transition velocity and greater than the friction transition velocity are defined in order to numerically integrate the equations of motion. These parameters are dependent on the material of bearing and types of lubricant used.
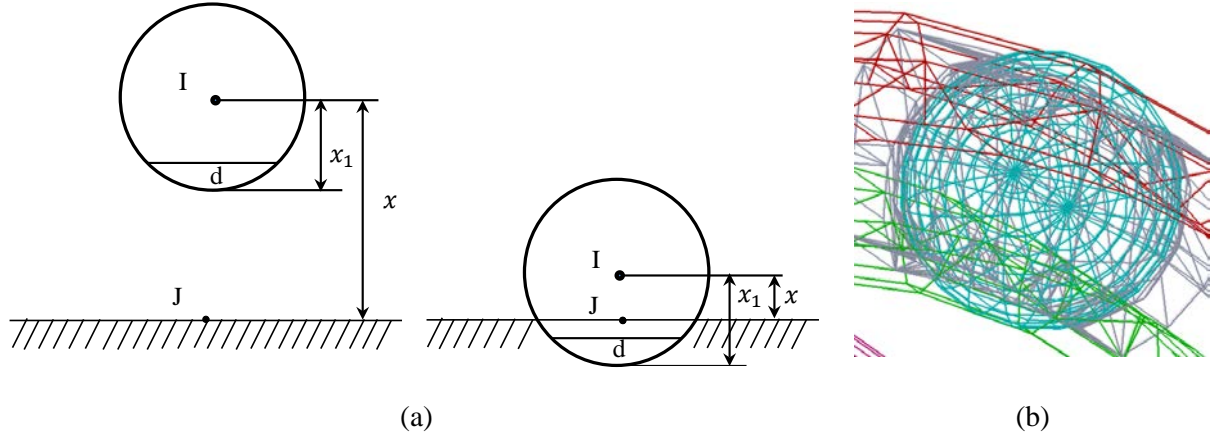
Fig. 17. (a) Example describing the solid-to-solid contact model in ADAMS [41] and (b) wireframe model of a ball with a part of the cage and races showing the nodes used in the discretized model for contact detection.

As an illustration, the normal contact force between a sphere and a flat surface is calculated using the Adams solver [41] as (see Fig. 17 (a))

$$F = \begin{cases} \max(0, K(x_1 - x)^e - STEP(x, x_1 - d, R, x_1, 0)\dot{x}) & \text{if} \quad x < x_1, \\ 0 & \text{if} \quad x \geq x_1, \end{cases} \tag{37}$$

where d, x, x_1, R and e represent, respectively, the boundary penetration at which the ADAMS solver applies full damping, the distance variable that is used to compute an impact function, the stiffness of the boundary surface interaction, the free length of x (if x is less than x_1 then ADAMS calculates a positive value for the force), the maximum damping coefficient and exponent of the force deformation characteristic. ADAMS uses the slave node-master surface concept from finite element method (FEM) for contact detection. The nodes and surfaces used for this purpose are obtained by discretization of the volume of the rigid bodies. A sample discretization of the volume is shown in Fig. 17(b).

The friction/ traction force is calculated assuming that Coulomb force acts between the bodies. The coefficients of friction for every slip velocity are calculated by Adams solver using the four values of input, namely, static and dynamic coefficients of friction and static and dynamic transition velocities. This value is multiplied to the normal force to find the frictional force [41].

5.3. Modelling of faults

A number of models of rolling element bearing are available in literature where the localised faults are modelled as small notches of triangular or rectangular shape. In reality, however, the imperfections that occur in industrial applications are not of regular geometry. However, the shape of the fault does not change the fault diagnosis schemes in frequency domain analysis, e.g. vibration analysis. Faults can be modelled in CAD geometry of inner race, outer race and ball by cutting of different types of slots or sections. In the present analysis, the regular faults in the outer race, inner

race and ball are modelled as shown in Figs. 18 (a), (b) and (c), respectively. These are exactly the same faults in the faulty bearings supplied with MFS system, which has been used in the experiments. The 3-D multi-body deep groove ball bearing model has the same geometric parameters of Rexnord MB-ER-16K ball bearing used in the MFS system.

<div align="center">(a)   (b)   (c)</div>
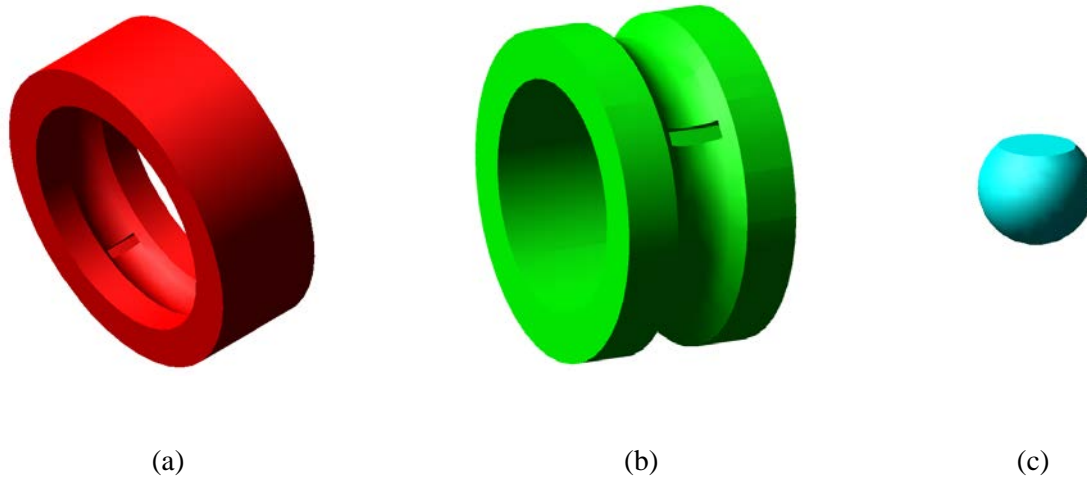
Fig. 18. CAD model of fault in (a) outer race, (b) inner race and (c) ball

5.4. Simulation set up and model validation

ADAMS models implementing different types of faults were simulated and the acceleration signals along vertical direction of pedestal (load zone direction) were collected as fault signatures. The data are collected for 10 seconds time window with a preferred step size of 0.0001 second. In all the simulations, the rotor is given a constant angular speed of 10 Hz. The simulation results were exported to MATLAB for post processing. ADAMS does not always produce time series data in ascending order and with fixed sampling interval. Thus, data are sorted and resampled in MATLAB before analysis.

The contact parameters, pedestal stiffness and damping are given in Table 4. The dimensions of the different parts are chosen in such a way that the total mass of the bearing is approximately equal to the original mass of the bearing used in the experiments. The mass (assuming steel material) of ball, inner race, outer race, cage and loader are obtained as 2.0446×10^{-3}, 67.697×10^{-3}, 141.254×10^{-3}, 14.201×10^{-3} and 5.063 kg, respectively, from the solid models. For nine balls, this gives a bearing weight (combining nine balls, cage, inner and outer races) of 241 grams, which is close to the weight of the actual bearing (See Fig. 19).

Table 4. Parameter values used in MBS-ADAMS model

Parameters	Values
Contact stiffness (K)	: 1.0×10^{11} N/m.
Contact damping (R)	: 20 Ns/m.
Static coefficient of friction (μ_S)	: 0.8.
Dynamic coefficient of friction (μ_k)	: 0.76.
Force exponent (e)	: 2.2.
Boundary penetration	: 1.0×10^{-5} m
Pedestal stiffness K_P	: 1.0×10^{10} N/m.
Pedestal damping (R_P)	: 1000 Ns/m.
Pedestal bushing stiffness (K_x, K_y, K_z)	: 1.0×10^{10} N/m.
Pedestal bushing damping (R_x, R_y, R_z)	: 1000 Ns/m.
Coupling stiffness (K_x, K_y, K_z)	: 1.0×10^{5} N/m.
Coupling damping (R_{cx}, R_{cy}, R_{cz})	: 1 Ns/m.

Fig. 19. Rexnord MB-ER-16K deep groove ball bearing

A sample result for constant frequency rotor (10 Hz) supported by a faulty bearing, in which one ball has fault and rest eight balls are good, is given in Fig. 20. Initially, the inner race has spin and all other bodies are stationary (zero initial conditions). This sets up transients in the beginning which steady after some time. It is noticed from Fig. 20 that there is a persistent loss and gain of contact at the starting and ending of fault. In fact, the ball may or may not be in contact with inner or outer race in unloaded zone. In Fig. 20, the frequency of inner race (rotor speed), cage, the faulty ball and one of the good balls (from remaining eight balls) are denoted by f_s, f_c, f_{bf} and f_{bg}, respectively. The spikes in the response of the faulty ball are due to large amount of impulsive forces which are generated when the traction is lost or regained between the ball and races. The speed profile of ball with no defect does not show such effects; the minor speed deviations are due to the impact forces from the loose ball carried to the rest of the system and transmitted to the good ball. Therefore, the element defect frequency (EDF) or ball spin frequency (BSF) which is generally observed in signal of previously simulated mathematical models for bearing with ball fault is absent in corresponding simulated ADAMS model. This is due to the fact that most of the mathematical models wrongly consider tractions between races and balls at all operating conditions and faults. In real practice, EDF

and BSF are not seen in frequency spectra of experimental signals from bearings with ball faults. In fact, ADAMS model does a more faithful representation of real system dynamics. The theoretically calculated cage and ball frequencies at shaft speed $f_s = 10\text{Hz}$ are $f_c = \frac{D-d}{2D}f_s \approx 3.99$ Hz and $f_b = \approx -\frac{D-d}{2d}f_s \approx -19.97$ Hz, respectively. ADAMS simulation in Fig. 20 shows nearly the same values. This validates the ADAMS model from kinematics viewpoint.
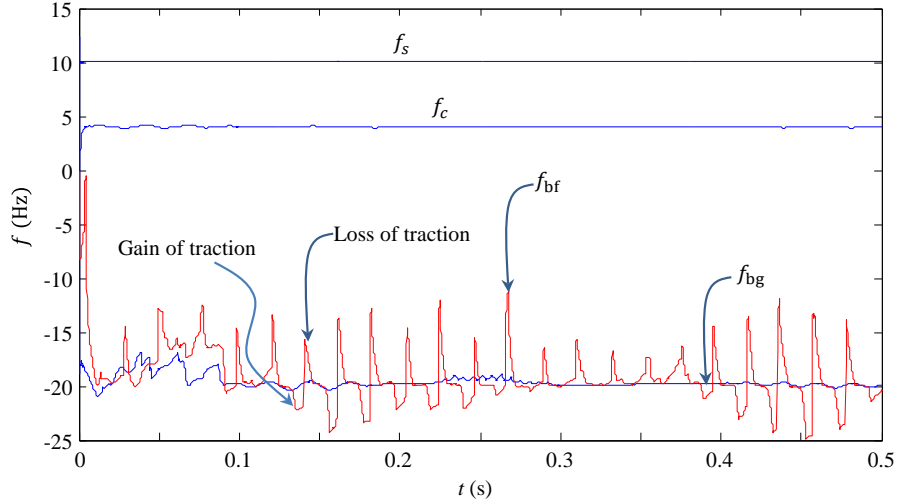
Fig. 20. Simulation results for one ball fault in a bearing using ADAMS MBS model. Note that ball speed is negative because balls rotate in opposite direction to the inner race and the cage.

6. Diagnosis scheme

The conventional method like Fast Fourier Transform (FFT) is unsuitable to clearly expose the BCFs in the frequency spectrum when the energy content in the range of BCFs is low and the noise is dominant. So, the signal dominated by noise needs to be processed using different techniques before analysis. Therefore, we perform envelope analysis in this article.

Envelope Analysis is a widely used enveloping or demodulation technique in machinery fault diagnosis. It is carried out using the following steps [42, 43].

1. Select a data collector whose dynamic range is large enough to observe several orders of fundamental frequency so that periodic content in the signal which is buried in the noise can be extracted.

2. The signal is then passed through a band pass filter with frequency range determined by fundamental frequency of interest, i.e., in the region of structural resonance, where there is high signal-to-noise ratio (SNR) and this frequency must be less than low frequency cut-off of the filter.

3. The filter captures a time block of signal in the specified frequency range and the block of data is then processed by high pass filtering, rectification, low pass filter and then modulated by Hilbert transform to keep only the envelope.

4. Finally, the signal is converted into a frequency spectrum of the envelope by FFT (Fast Fourier Transform), called envelope spectrum, to identify fault in the demodulated signal.

The steps 2 to 4 are easily performed with the help tools available in MATLAB$^{®}$.

Note that the enhanced signal amplitudes are the result of summation of energies in the filter band and are not comparable with normal acceleration levels in original vibration signal. However, the signal is passed through the same filter band each time and thus any increase or decrease of fault size will correspondingly increase or decrease the signal strength of that band. The harmonics of damage frequencies in the FFT is due to degradation of bearing and, if the side bands are more pronounced then the damage progression is more [42].


7. Results and discussion

The Rexnord MB-ER-16K $1''$ deep groove ball bearing has following geometric data: ball radius 3.97 mm, pitch diameter 39.32 mm, number of balls n_b=9 and contact angle zero. This bearing is used in the experiments and the corresponding bearing geometry data are also used in the simulations. Using these geometric parameters, the bearing characteristics frequencies (See Section 3.0) are calculated as: FTF $\approx 0.399\,f_s$, BPFO $\approx 3.591\,f_s$, BPFI $\approx 5.408\,f_s$ and BSF $\approx 2.375 f_s$. The other parameters assumed while developing the models are given in the respective sections where the models are described. Experimental as well as simulated data are collected at a sampling frequency of 50000 for 10 seconds duration for analysis purpose.
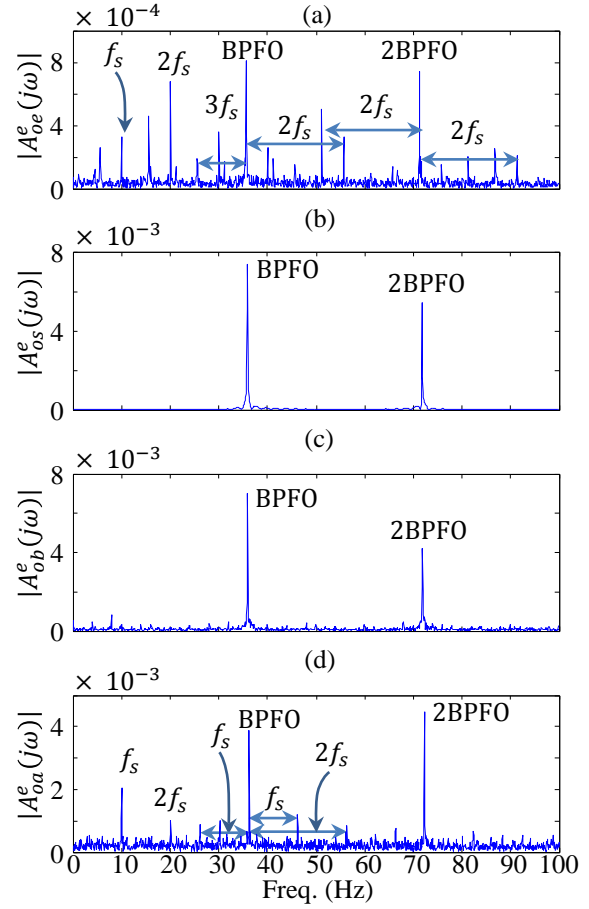
The normalized vibration signals of pedestal for bearing with outer race fault for different analysis are denoted by A_{oe}, A_{os}, A_{ob} and A_{oa}, where the first subscript indicates the type the fault type (here, o for outer race fault) and the second subscript indicates the source of the signal, i.e., e for experiment, s for Simulink model, b for bond graph model, and a for ADAMS model. The envelope spectrums of the corresponding signals are denoted by $A_{oe}^e(j\omega)$, $A_{os}^e(j\omega)$, $A_{ob}^e(j\omega)$ and $A_{oa}^e(j\omega)$, respectively, where the superscript e indicates envelope of the signal. Zoomed portions (one second time window) of the experimental and simulated MATLAB-Simulink, bond graph and ADAMS MBS signals for bearing with outer race faults are shown in Figs. 21 (a), and (b), (c) and (d), respectively. The corresponding envelope spectra of the signals are shown in Figs. 22 (a) and (b), (c) and (d), respectively.

BPFO and its harmonics are exposed in all the envelope spectra (simulated as well as experimental signals). The primary differences between all the envelope spectra is that the shaft frequency and its

harmonics can be observed in the case of experimental signal and simulated ADAMS MBS; and the side bands can also be observed in those two cases. Thus, ADAMS MBS model gives a result which is more consistent with the experimental results.
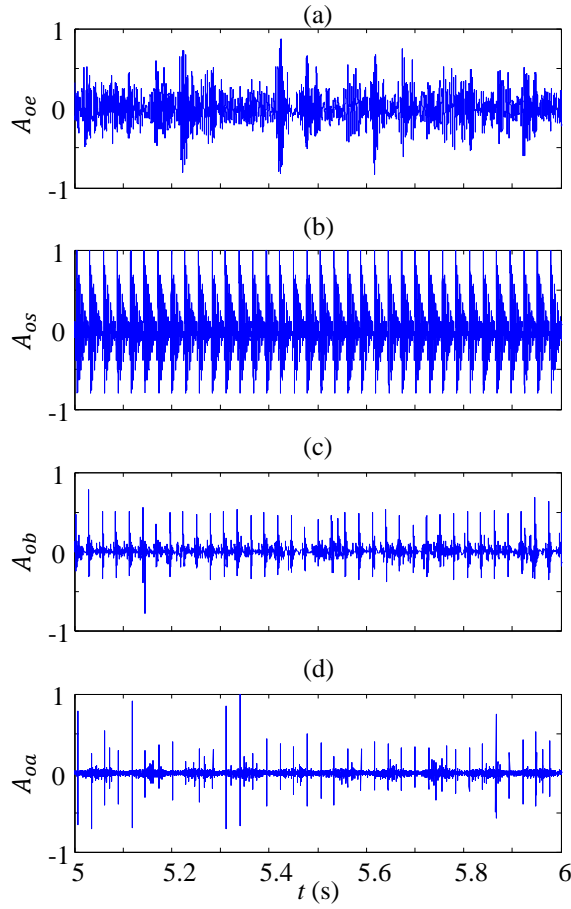
Fig. 21. A zoomed portion of normalized vibration signals: (a) experimental, and (b) 5-DOF Simulink, (c) bond graph and (d) ADAMS MBS simulated signals for bearing with outer race fault.
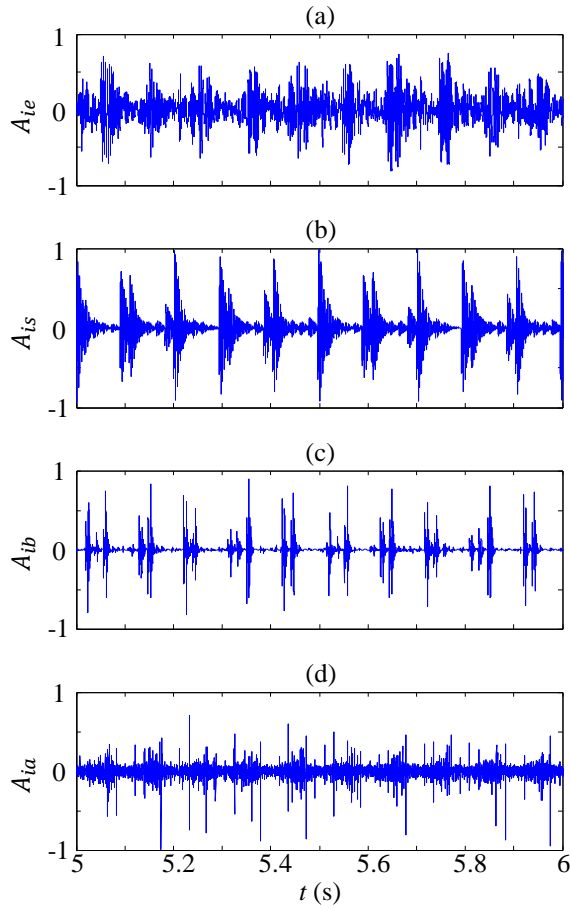
Fig. 22. Envelope spectra of vibration signals for bearing with outer race fault: (a) experimental, and (b) 5-DOF Simulink, (c) bond graph and (d) ADAMS MBS simulation.
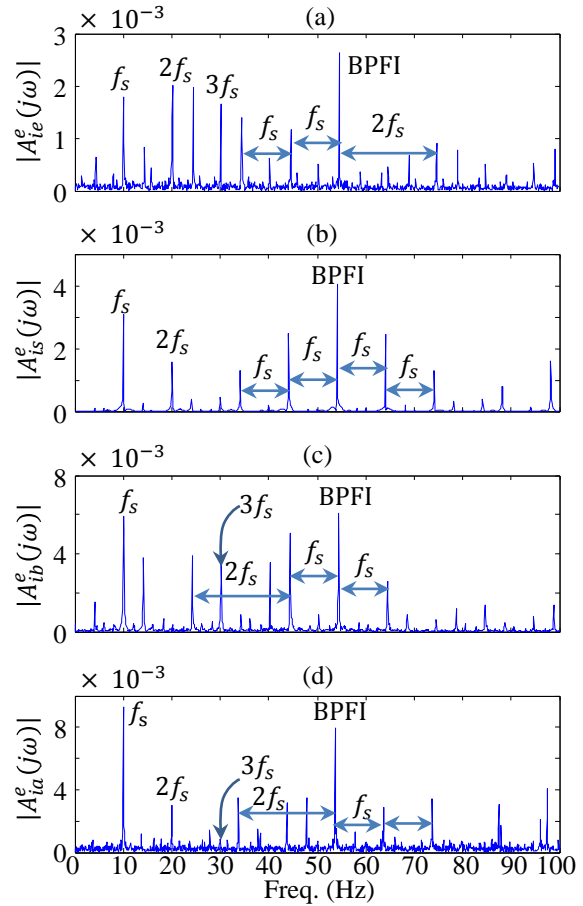
The normalized vibration signals for bearing with inner race fault for different analysis are denoted by A_{ie}, A_{is}, A_{ib} and A_{ia}, respectively, where the first subscript i indicates the fault type and the second subscript indicates the source of the signal as defined earlier. These signals in one second time window are shown in Fig. 23. The envelope spectra of the corresponding signals are shown in Fig. 24. It is seen from these envelope spectra that BPFI, shaft frequency and its harmonics, and side bands are exposed in all the envelope spectra, i.e., of simulated as well as experimental signals. Therefore, no clear conclusions can be made regarding superiority of any of the models.

Zoomed portion (one second) of normalized vibration signals for bearings with ball fault are shown in Fig. 25. The signals are denoted by A_{be}, A_{bs}, A_{bb} and A_{ba}, where the first subscript b indicates the type of fault and the second subscript indicates the source of the signal (experiment and various models) as discussed earlier. The envelope spectra of the corresponding signals for bearing with ball faults are shown in Fig. 26. It is observed that only the cage frequency (or FTF) and its harmonics are exposed in the envelope spectrum of experimental signal. In addition to cage frequency and its harmonics, BSF and EDF are exposed in the envelope spectrum of simulated 5-DOF Simulink signal and EDF and its harmonics with side bands spaced at cage frequency are exposed in the simulated bond graph signal. In the envelope spectrum of MBS ADAMS simulated signal, only the cage frequency and its harmonics are exposed clearly and a small peak appears at EDF. A clear similarity in the envelope spectra of experimental and MBS ADAMS simulated signals can be established. The spectra of simulated signals from the other two models are far away from that of experimental results. It can be concluded that MBS ADAMS model is a more faithful representation of the real rotor bearing system with ball faults.
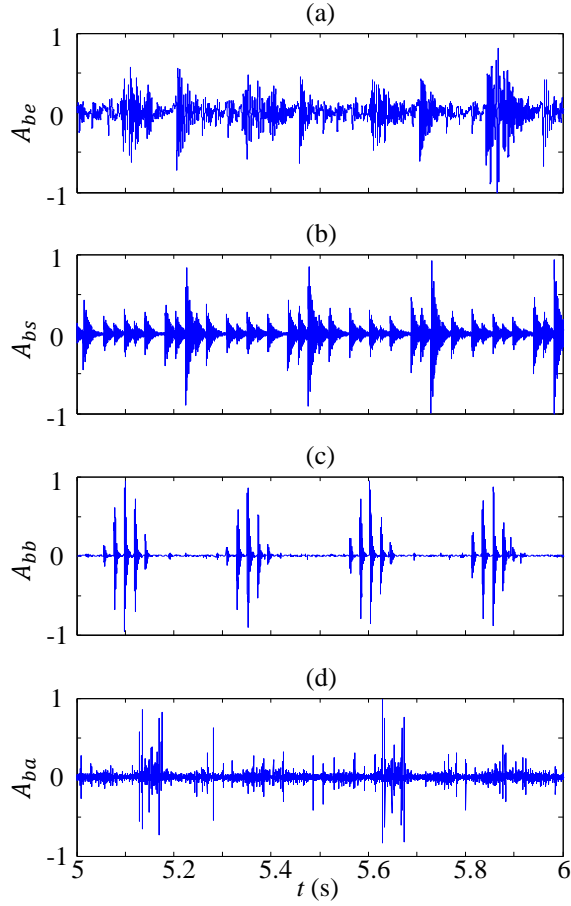

Fig. 23. A zoomed portion of normalized vibration signals for bearings with inner race fault: (a) experimental, and (b) 5-DOF Simulink, (c) bond graph and (d) ADAMS MBS simulated.
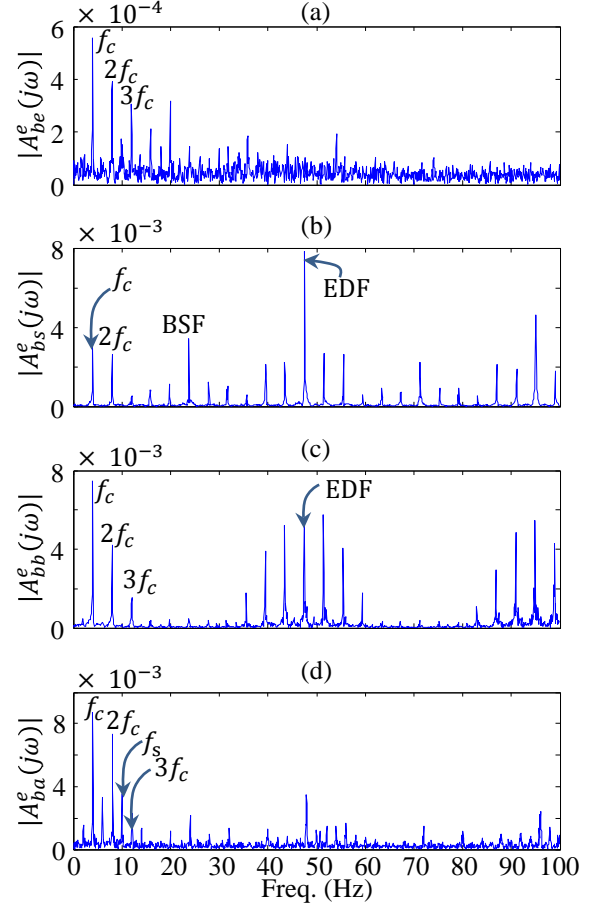
Fig. 24. Envelope spectra of vibration signals for bearings with inner race fault: (a) experimental, and (b) 5-DOF Simulink, (c) bond graph and (d) ADAMS MBS simulated.

Table 5 shows a summary of different major frequencies and side bands of the envelope spectra of different faulted bearings when the signal is obtained from different sources considered here. It can be inferred that the envelope spectra of experimental analysis is more consistent with the simulation results of MBS ADAMS. Though the simulation results of other models are good enough to show the symptoms of bearing faults, MBS ADAMS model outperforms them. Moreover, MBS ADAMS model due to its design flexibility can be used to predict the fault symptoms of bearing under different types of geometrical imperfections and loading conditions.

Fig. 25. A zoomed portion of normalized vibration signals for bearing with ball fault: (a) experimental, and (b) 5-DOF Simulink, (c) bond graph and (d) ADAMS MBS simulated.
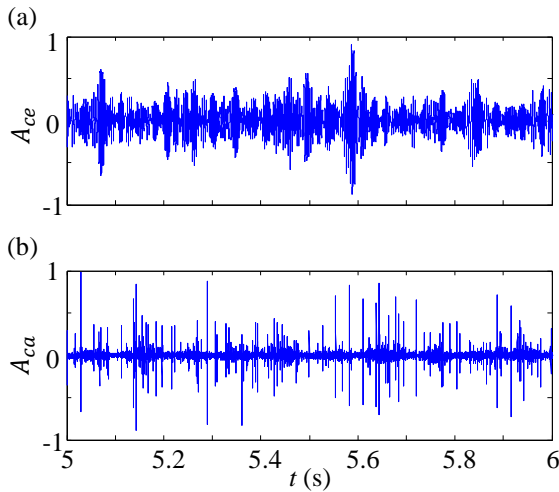
Fig. 26. Envelope spectra of vibration signals for bearing with ball fault: (a) experimental, and (b) 5-DOF Simulink, (c) bond graph and (d) ADAMS MBS simulated.

Table 5. Summary of major frequency bands and side bands under different types of defects

Types of analysis	Outer race fault		Inner race fault		Ball fault	
	Major bands	Side bands	Major bands	Side bands	Major bands	Side bands
Experiment	BPFO, f_s and its harmonics	f_s, $2f_s$	BPFI, f_s and its harmonics	f_s, $2f_s$	f_s, f_c and its harmonics	−
5-DOF Simulink	BPFO and its harmonics	−	BPFI, f_s and its harmonics	f_s, $2f_s$	BSF, EDF, f_c and its harmonics	f_c
Bond graph	BPFO and its harmonics	−	BPFI, f_s and its harmonics	f_s, $2f_s$	EDF, f_c and its harmonics	f_c
MBS ADAMS	BPFO, f_s and its harmonics	f_s, $2f_s$	BPFI, f_s and its harmonics	f_s, $2f_s$	f_s, f_c and its harmonics	−

To show the flexibility of the ADAMS MBS model, we consider a case of combination faults. The normalized amplitude signals with first subscript c indicate combination fault and the second subscript, as usual, indicates the source of the signal (experiment or model). Figure 27 shows the simulated vibration signal of pedestal and its envelope spectrum using ADAMS MBS model. The BPFO and its harmonics, BPFI and cage frequency and its harmonics are exposed in the envelope spectrum. Many other geometrical imperfections such as elliptical ball, elliptical cage, oversized ball, cage run-out and combinations of different imperfections can be easily incorporated in the ADAMS MBS model to interpret the frequency domain characteristics of bearings by simply modifying the solid models of the various parts of the bearing.

Fig. 27. A zoomed portion of normalized vibration signals for bearing with combination fault: (a) experimental, and (b) ADAMS MBS simulated.
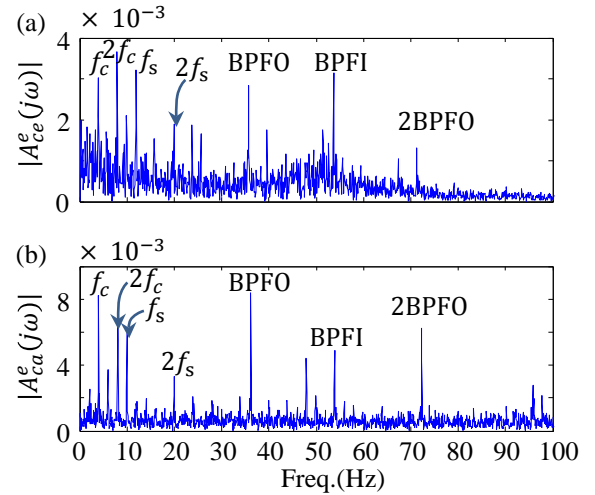
Fig 28. Envelope spectra of vibration signals for bearing with combination fault: (a) experimental, and (b) ADAMS MBS simulated.

8. Conclusions

Three different models of rolling element bearings, namely, a 5- DOF model in MATLAB-Simulink environment, a bond graph model and a model in MBS software ADAMS are developed and validated with experiments. These models can thus serve as data generators for development and testing of bearing fault diagnostic tools.

The contributions can be summarised as

- The MATLAB model is the simplest of all and yet is able to model fault symptoms quite well for constant high speed rotor operation.

- The bond graph and ADAMS models include cage dynamics effect.

- The ADAMS model allows for simulation of very complex fault scenarios. It is very easy to construct and does not require mathematical understanding of the problem. The developed ADAMS and bond graph models can be interfaced with various rotor dynamics and drive motor models.

- The bond graph and ADAMS models are able to simulate the effect of loose balls (clearance effect).

- The developed bond graph model is a multi-body model, but can also be a multi-energy domain model by virtue of the properties of bond graph. It is a modular model which can be modified and extended. The model can be interfaced with available models of various electrical drives (DC motor, induction motor, etc.), rotor dynamic systems (flexible rotor, multi-disk rotor, geared and splined shafts, etc.) and bearings. The developed bond graph model can also be extended to include other factors like thermal and hydrodynamic effects such as in journal bearings.

- The simulation of the 5-DOF Simulink and bond graph models reveal that faults in rolling elements cause clear periodic impacts at BSF whereas such features are obscure in the experimental data. Thus, the contact, traction and preload modelling need significant improvement. The simulation of ADAMS MBS model reveals loss of contact in unloaded zones resulting in significant change of ball spin velocity and thus, justifies why BSF and EDF are absent in the frequency spectra of experimental signals.

- The ADAMS model of the ball bearing developed in this work is the first such reported numerical model and can be extended for simulating complex ball bearing faults such as oversized ball, elliptical ball, and elliptical cage, etc.

References

1. N. Tondon, A. Choudhury, A review of vibration and acoustics measurement methods for the detection of defects in rolling element bearing, Tribology International 32 (1999) 469-480.

2. A.K.S. Jardine, D. Lin, D. Banjevic, A review on machinery diagnostics and prognostics implementing condition-based maintenance, Mechanical Systems and Signal Processing 20 (2006) 1483–1510. doi:10.1016/j.ymssp.2005.09.012.

3. P.D. McFadden, J.D. Smith, Vibration monitoring of rolling element bearings by the high-frequency resonance technique - a review, Tribology International 17 (1984) 3–10. doi:10.1016/0301-679X(84)90076-8.

4. Y.T. Su, S. J. Lin, On initial fault detection of a tapered roller bearing: Frequency domain analysis, Journal of Sound and Vibration 155 (1992) 75-84. doi:10.1016/0022-460X(92)90646-F.

5. P.D. McFadden, M.M. Toozhy, Application of synchronous averaging to vibration monitoring of rolling element bearings, Mechanical Systems and Signal Processing 14 (2000) 891–906. doi:10.1006/mssp.2000.1290.

6. J. Antoni, R.B. Randall, The spectral kurtosis: application to the vibratory surveillance and diagnostics of rotating machines, Mechanical Systems and Signal Processing 20 (2006) 308–331. doi:10.1016/j.ymssp.2004.09.002.

7. I.M. Howard, Higher-order spectral techniques for machine vibration condition monitoring, Proc. Inst. Mech. Eng. Part G Journal of Aerospace Engineering 211 (1997) 211–219. doi:/10.1243/0954410971532622.

8. S. Prabhakar, A.R. Mohanty, A.S. Sekhar, Application of discrete wavelet transform for detection of ball bearing race faults, Tribology International 35 (2002) 793-800. doi:10.1016/S0301-679X(02)00063-4.

9. N.G. Nikolaou, A. Antoniadis, Rolling element bearing fault diagnosis using wavelet packets, NDTE International 35 (2002) 197–205. doi:10.1016/S0963-8695 (01)00044-5.

10. C. Mishra, A. K. Samantaray, G. Chakraborty,   Rolling element bearing defect diagnosis under variable speed operation through angle synchronous averaging of wavelet de-noised estimate, Mechanical Systems and Signal Processing 72-73 (2016) 206-222. doi:10.1016/j.ymssp.2015.10.019.

11. G.F. Bin, J.J. Gao, X.J. Li, B.S. Dhillon, Early fault diagnosis of rotating machinery based on wavelet packets—Empirical mode decomposition feature extraction and neural network, Mechanical Systems and Signal Processing 27 (2012) 696-711. doi:10.1016/j.ymssp.2011.08.002.

12. P.K. Gupta, Advanced dynamics of rolling elements, Springer-Verlag, Berlin, 1984.

13. P.K. Gupta, Current Status of and Future Innovations in Rolling Bearing Modeling, Tribology Transactions 54 (2011) 394–403. doi:10.1080/10402004.2010.551805.

14. C.T. Walters, The Dynamics of Ball Bearings, Journal of Tribology 93 (1971) 1–10. doi:10.1115/1.3451516.

15. P.K. Gupta, Dynamics of rolling element bearings part I-IV, Journal of Tribology 101 (1979) 293-326.

16. L.E. Stacke, F. D., P. Nordling, BEAST- A Rolling Bearing Simulation Tool, Proc. IMechE Part K: Journal of Multi-Body Dynamics 213 (1999) 63–71. doi:10.1243/1464419991544063.

17. A. Ashtekar, F. Sadeghi, L.E. Stacke, A new approach to modeling surface defects in bearing dynamics simulations, Journal of Tribology 130 (2008) 041103. doi:10.1115/1.2959106.

18. F. Wang, M. Jing, J. Yi, G. Dong, H. Liu, and B. Ji, Dynamic modelling for vibration analysis of a cylindrical roller bearing due to localized defects on raceways, Proc IMechE Part K: Journal of Multi-body Dynamics 229 (2015) 39–64. doi:10.1177/1464419314546539.

19. O. Cakmak, K.Y. Sanliturk, A dynamic model of an overhung rotor with ball bearings, Proc. Inst. Mech. Eng. Part K Journal of Multi-Body Dynamics 225 (2011) 310–321. doi:10.1177/1464419311408949.

20. T. Sakaguchi, K. Harada, Dynamic Analysis of Cage Behavior in a Tapered Roller Bearing, Journal of Tribology 128 (2006) 604–611. doi:10.1115/1.2197527.

21. http://handle.dtic.mil/100.2/ADA042981 (accessed 21 February 2017).

22. http://www.bearingspecialists.com/software.asp (accessed 21 February 2017).

23. P.K. Gupta, Transient Ball Motion and Skid in Ball Bearings, Journal of Tribology 97 (1975) 261–269. doi:10.1115/1.3452568.

24. R.J. Kleckner, J. Pirvics, V. Castelli, High Speed Cylindrical Rolling Element Bearing Analysis "CYBEAN" Analytic Formulation, Journal of Tribology 102 (1980) 380–388. doi:10.1115/1.3251553.

25. L. Houpert, CAGEDYN: A Contribution to Roller Bearing Dynamic Calculations Part I: Basic Tribology Concepts, Tribology Transactions 53 (2009) 1–9. doi:10.1080/10402000903132093.

26. M. Nakhaeinejad, M.D. Bryant, Dynamic modeling of rolling element bearings with surface contact defects using bond graphs, Journal of Tribology 133 (2010) 011102 (1–12). doi:10.1115/1.4003088.

27. C. Mishra, A. K. Samantaray, G. Chakraborty, Bond graph modelling and experimental verification of a novel scheme for fault diagnosis of rolling element bearings in special operating conditions, Journal of Sound and Vibration 377 (2016) 302–330. doi:10.1016/j.jsv.2016.05.021

28. N. Sawalhi, R.B. Randall, Simulating gear and bearing interactions in the presence of faults: Part I. The combined gear bearing dynamic model and the simulation of localised bearing faults, Mechanical Systems and Signal Processing 22 (2008) 1924–1951. doi:10.1016/j.ymssp.2007.12.001.

29. W. Borutzky, Bond Graph Methodology: Development and Analysis of Multidisciplinary Dynamic System Models, Springer, London, 2010.

30. A. Mukherjee, R. Karmakar, A.K. Samantaray, Bond Graph in Modelling, Simulation and Fault Identification, CRC Press, Florida, 2006.

31. R. Merzouki, A.K. Samantaray, P.M. Pathak, B. Ould Bouamama, Intelligent Mechatronic Systems: Modeling, Control and Diagnosis, Springer, London, 2012.

32. G. Dauphin-Tanguy, Les bond graphs. Hermes Science Europe Ltd., Paris, 2000.

33. T. A. Harris, M. N. Kotzalas, Rolling Bearing Analysis: Essential concept of Bearing Technology (Fifth edition), CRC press, New York, 2007.

34. MathWorks, Simulink Documentation, https://www.mathworks.com/help/simulink/ (accessed 21 February 2017).

35. S.T. Karris, Introduction to Simulink with Engineering Applications, 3rd Ed., Orchard Publications, CA, 2011.

36. S. Khanam, J. K. Dutt, N. Tandon , Impact force based model for bearing local fault identification, Journal of Vibration and Acoustics 137 (2015), 051002-051013. doi:10.1115/1.4029988.

37. C. Mishra, G. Chakraborty, A. K. Samantaray, Rolling element bearing fault modelling to develop a diagnosis scheme for oscillating and non-uniform shaft rotation, Procedings of INACOMM2013, Roorkee, December 2013, pp. 86-94.

38. B. Ould Bouamama, AK Samantaray, K Medjaher, M Staroswiecki, G. Dauphin-Tanguy, Model builder using functional and bond graph tools for FDI design, Control Engineering Practice 13 (7) (2005) 875–891.

39. A Mukherjee, AK Samantaray, System modelling through bond graph objects on SYMBOLS 2000, Proceedings of International Conference on Bond Graph Modeling and Simulation (ICBGM 2001), Simulation Series 33 (1), 164–170, January 7–10, Phoenix, AZ, 2001.

40. A Mukherjee, AK Samantaray, SYMBOLS Shakti User's Manual, High-Tech Consultants, STEP, Indian Institute of Technology, Kharagpur, 2005.

41. MSC ADAMS reference manual, MSC Software Corp., California, USA, 2012. Internet: www.mscsoftware.com/product/adams, last accessed: 21 February 2017.

42. J. Courrech, Envelope analysis for effective rolling element fault detection-facts or fiction?, Uptime Magazine 8 (1) (2000) 14–17.

43. R. M. Jones, Enveloping for bearing analysis, Sound and Vibration 30(2) (1996) 10-15.